Table of Content

1. Introduction

1.1 Background

Understanding surface water runoff during rainfall is increasingly imperative in urban area.

Since the industrial revolution in the late 18th century, brick, cement and asphalt have gained wide popularity as building materials due to their inexpensiveness: they are laid on ground to create smoother surface for the convenience of cars and pedestrians. However, unlike natural grassland and open-pit areas, they are significantly more impermeable, sealing rainwater from seeping into the ground. Coupled with the growing proportion of world's population living in urban areas, many towns and cities are expanding, causing more lands to be sealed off and increasing the risk of flooding when it rains. Concurrently, global warming is predicted to result in more extreme weathers, bringing heavier precipitations to some flood-prone urban areas. Take, for instance, it is estimated that the heavily soil-sealed UK will experience more days of heavy rainfall beyond year 2071 (European Environment Agency, 2012), as shown in Figure 1. Bearing in mind the huge economy and social costs of urban flooding such as the £3.2 billion loss in the 2007 UK summer flood (Pitt Review, 2008), these issues call for the urgency for a sustainable urban planning which includes careful design of drainage system.

At the same time, the extensive development in computer and numerical analysis provides exciting opportunity to simulate rainfall-runoff processes, which can then be used to evaluate the effectiveness of drainage system design. Moreover, if spatial rain intensity data from digital rain gauges is available, flood occurrence can be predicted in real-time. These are possible provided that the rainfall-runoff processes are well understood, and the numerical model for the simulation is rigorously tested for its reliability.

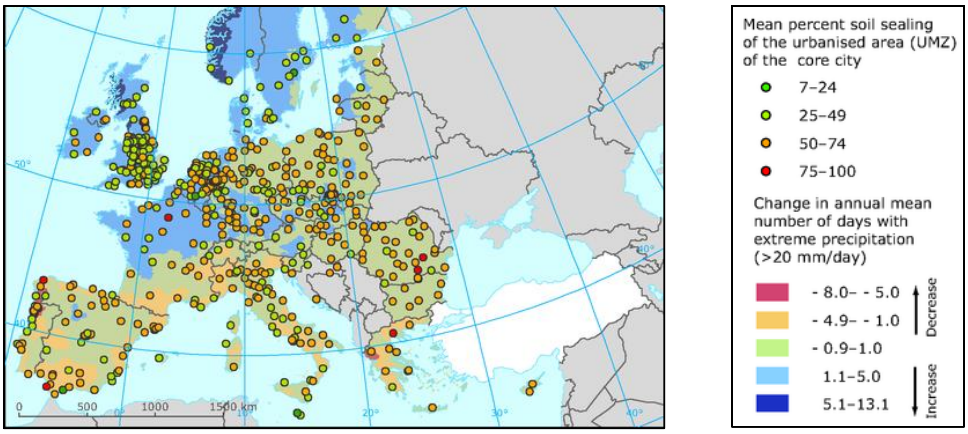

Figure 1: Average soil sealing degree and change in annual number of days with heavy rainfall between 2071-2100 (with reference to 1961-1990)

1.2 Previous research

Rainfall-runoff processes have been a topic for research for more than half a century. Before the invention of modern computer, Iwagaki (1955) derived an approximate method for calculation of unsteady flow in one-dimensional (1D) open channels using characteristic curves. He then compared his numerical results with his physical experiments by simulating uniform precipitation on a three-slope laboratory flume; both results are in good agreement. Subsequently, Zhang and Cundy (1989) simulated Iwagaki's experiments using a finite-difference two-dimensional (2D) shallow water model and obtained comparable results. Further physical experiments and simulations were conducted by Cea et al. (2008); he successfully validated the application of shallow water model over a simple 2D geometry that involves two walls on three-slope terrain.

2D shallow water models are popular for surface runoff in urban areas due to the lack of field data needed to build detailed three-dimensional (3D) model and its high computational costs (Cea et al, 2009). Three modelling techniques are commonly used to solve 2D shallow water models: the kinematic wave, diffusive wave and dynamic wave approximations. Ponce (1991) showed that the non-diffusive feature of kinematic waves caused the frequent formation of the kinematic shock, which is actually rare in practice. He also concluded that the dynamic models properly account for the dynamic effect, and was particularly suitable for flow that was near-critical and supercritical. Cea et al. (2009) compared numerical results from diffusive wave and dynamic wave models with 72 physical experiments, and concluded that depth-averaged dynamic wave approximations are more suitable for predicting rainfall-runoff in urban environments.

1.3 Present research

It is common to use the empirical Manning coefficient to model the roughness of runoff surface in research; in fact, Manning coefficient is used in all numerical models in those researches aforementioned. Therefore, the first part of this project attempts to study the effect of using different methods to model surface roughness. Results from physical experiments by Iwagaki and Cea et al. will be used to validate and compare the results from any numerical analysis.

The second part focuses on the understanding of how arrangement of buildings influences rain-induced flooding.

In line with conclusions drawn from previous researches, a programme that features two dimensional shallow water model that uses depth-averaged dynamic wave approximations is used for all numerical analyses in this project. These techniques will be further explained in later sections of this report.

1.4 Objectives

There are two main objectives of the project:

1. Propose and study an alternative scheme to model bed friction using surface roughness height k_s

The first step involves derivation of an analytical relationship between k_s and Chezy coefficient, a coefficient that links flow speed and terrain. This relationship was then coded into the 2D shallow water model. Next, a total of 30 chosen physical experiments from Iwagaki (1955) and Cea et al. (2008, 2009) were simulated numerically using the modified model, with the aim to find k_s that best fits the experimental data. These results were also compared to those from numerical simulations using Manning coefficient.

2. Study the effect of building area ratio on time of concentration T_c for multiple buildings arrangement

Building area ratio (BA) is defined as the ratio of area occupied by all buildings to the total catchment area. Previous researches had found that the positive correlation between build-up area ratio and T_C is different for regular, random and staggered buildings layout (Liang, 2016), as shown in Figure 2 and 3. This project attempts to explain such difference in correlation by performing 100 additional numerical simulations on 100 buildings. More inferences were drawn from the combined results of these simulations and those from previous researches.

The next chapter of this report will focus on explaining in depth the necessary theoretical background associated with these objectives, followed by exploring the 2D shallow water numerical model used in conducting this project.

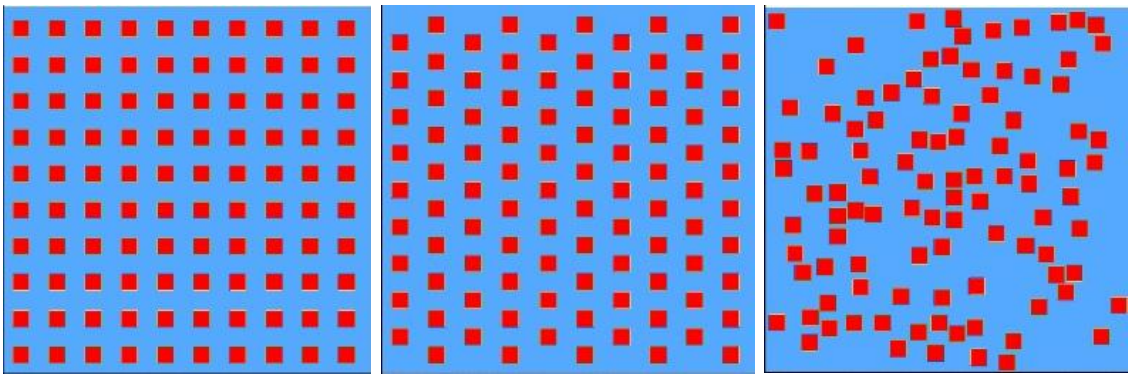

Figure 2: Regular, staggered and random array of 100 buildings. Each red square block indicates the plan location of a building

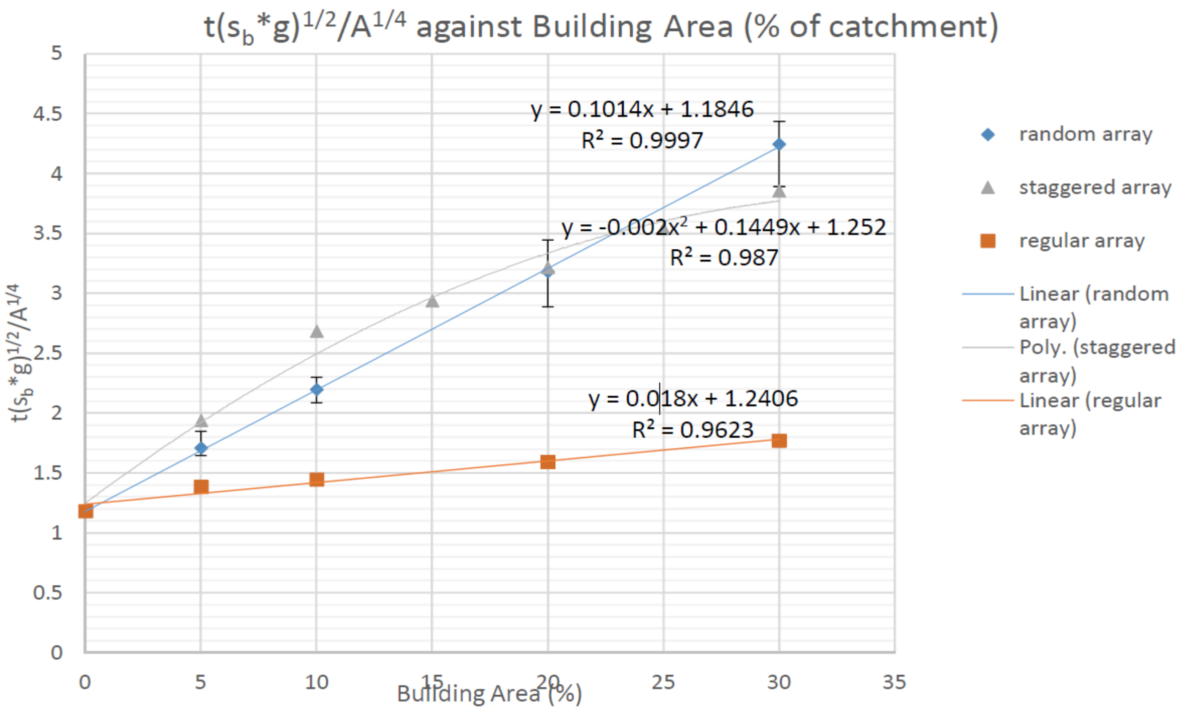

Figure 3: Relationship between BA and time of concentration T_c, plotted using non-dimensionalised T_c (Lam, 2016)

2. Theoretical Background

2.1 Unit hydrograph theory

Rainfall over a catchment will produce an outflow from the catchment that contains mixed information about the rainfall and the hydrological nature of the catchment. However, if a fixed rainfall is applied to different catchments, the resulting discharge patterns are then comparable as the effect of characteristics hydrology of those catchments is isolated from the effect of rainfall. Therefore, the unit hydrograph theory utilises this convenience by applying a permanent rainfall uniform across time and the area of whole catchment from the beginning. This would produce an excess outflow hydrograph that achieves an equilibrium state, when the volumetric rate of rainwater introduced to the catchment equals the volumetric outflow rate. The time it happens is the time of concentration T_C, illustrated in Figure 4.

One of the key assumptions is that outflow hydrograph is directly proportional to the intensity of the rainfall; in reality, this principle is not valid. Rainwater can be discharged from a catchment via surface, subsurface or groundwater runoff; the proportion of those runoff components often changes depending on the size of rainfalls, even if they are of the same duration. In urban area, losses due to subsurface and groundwater runoff are often negligible due to the abundance of impervious surface (Ochoa-Rodríguez, 2013). Nonetheless, it is noteworthy that the rainfall in this project refers to the effective rainfall that results in any surface runoff, discounting other forms of losses and runoffs.

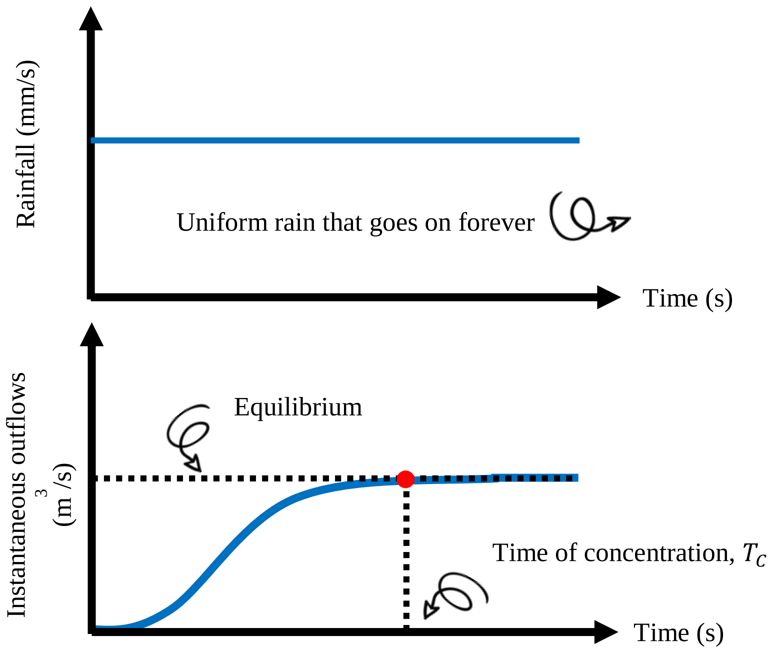

Figure 4: Unit hydrograph theory and time of concentration Tc

2.2 Wide channel flow theory

In a long channel where discharge is kept constant, uniform flow will develop at the middle section where slope and cross-sectional shape of channel is kept constant. In uniform flows, the frictional force acting upstream due to water flowing past rough surface of channel balances the component of self-weight of water acting downstream. Using force balance and assuming that the channel is much wider as compared to the depth of flow, the Chézy formula can be derived as:

$$U = C\sqrt{HS_b}$$

which links H, the water depth and S_b, the slope of the channel to the depth-averaged flow velocity, U using the Chézy coefficient, C. The value of C is a complex function of roughness of channel bed, degree of meandering of channel and flow conditions such as water depth. To estimate C, it is very common to apply the Manning formula, which is an empirical formula derived from experiments and takes the form:

$$C = \frac{h^{1/6}}{n}$$

where n is the Manning roughness coefficient and h is the water depth, assuming the channel is very wide. The values of n are estimated based on experimental data and field observations. However, Manning formula assumes the flow is in the hydraulically rough regime which the Reynolds number for the flow is large. While this remains valid for most real-world river flow, the application of Manning formula on numerical analysis of laboratory experiments can be debatable due to the relatively small Reynold-number flows.

An alternative parameter to describe the roughness of the channel is the equivalent roughness height, k_s. Despite its name, it encompasses other non-height effects of the roughness elements such as steepness, asymmetry, orientation and uniformity. Therefore, a rough wall can be thought as having an equivalent roughness height of k_s if it has the same influence on flow as a smooth wall covered with one layer of uniform sand of diameter k_s (Liang, 2015). The concept of k_s will be used in deriving an alternative method to estimate C, which will be discussed in detail in the beginning of Chapter 4.

3. Numerical Model

3.1 Shallow water equations

As this project was interested in the study of how the topography and arrangement of building affect the hydrograph and time of concentration T_c, the numerical model suitable for these simulations would need to capture the characteristics of unsteady open channel flow. Hence, the simple Chézy formula described in the previous chapter was not suitable. From the previous researches in Chapter 1, it was found that 2D shallow water equations (2D SWE) with depth-averaged dynamic wave application was particularly suitable for modelling urban flooding. They comprised of three equations, derived based on the principle of conservation of mass (Equation 1) and conservation of momentum in x-direction (Equation 2) and y-direction (Equation 3), as shown below:

$$\frac{\partial \eta}{\partial t} + \frac{\partial q_x}{\partial x} + \frac{\partial q_y}{\partial y} = 0 \qquad \textit{Equation 1}$$

$$\frac{\partial q_x}{\partial t} + \frac{\partial \left(\frac{\beta {q_x}^2}{H} \right)}{\partial x} + \frac{\partial \left(\frac{\beta q_x q_y}{H} \right)}{\partial y} = -gH \frac{\partial \eta}{\partial x} - \frac{g q_x \sqrt{{q_x}^2 + {q_y}^2}}{H^2 C^2} \qquad \textit{Equation 2}$$

$$\frac{\partial q_y}{\partial t} + \frac{\partial \left(\frac{\beta q_x q_y}{H} \right)}{\partial x} + \frac{\partial \left(\frac{\beta {q_y}^2}{H} \right)}{\partial y} = -gH \frac{\partial \eta}{\partial y} - \frac{g q_y \sqrt{{q_x}^2 + {q_y}^2}}{H^2 C^2} \qquad \textit{Equation 3}$$

Therefore, the unit width volumetric flow rate in x and y directions (q_x, q_y) and water depth above a datum level η can be solved numerically for each grid location (x, y) at time t, given a gravitational acceleration g and the Chezy coefficient C of the flow as defined in Chapter 2. The correction factor for the non-uniform vertical velocity profile is denoted as β, which can be set as 1.0 for a uniform velocity distribution and 1.016 for a seventh power law velocity distribution. Total water depth at each point is denoted as H, which can be calculated by summing η and the height of datum above plane (Liang, Lin & Falconer, 2006).

Some assumptions of the 2D SWE above were:

1. Small water depth H such that vertical momentum exchange was insignificant,
2. Incompressible runoff fluid,
3. No Coriolis effect due to rotation of Earth,
4. No viscous forces, and

5. No effects of wind,

The first four assumptions had negligible impact on the results of numerical analysis as both the laboratory models and actual urban flooding have much smaller water depth as compared to the length scale of the domain, and involve mostly water. Wind adds complexity to the problem and hence was not considered in this project.

Given the benefits of 2D SWE over a typical 3D scheme mentioned in previous researches in Chapter 1, it was decided that all numerical simulations in this project would be solved by a 2D SWE programme proposed by Liang et al. (2006).

3.2 Numerical scheme

To solve the non-linear 2D SWE described above numerically, a discretisation scheme that is computationally efficient, stable and reliable in both subcritical and supercritical flows is required.

It is found that schemes higher than first order will always produce spurious oscillations around discontinuities such as bores and hydraulic jumps (Harten, 1983). A solution to this is to include a total variation diminishing (TVD) step in those higher order schemes; it limits any oscillation through added artificial dissipation terms. Hence, by adding these diminishing terms into the corrector step of a typical MacCormack scheme, it allows the 2D SWE to be solved (Mingham, Causon & Ingram, 2001). This TVD-MacCormack scheme was validated against hypothetical and experimental dam break scenarios in previous papers.

One drawback is that the scheme is explicit; there is an upper limit to the time step and the resolution of domain to achieve convergence for solutions.

3.3 Time step and domain resolution

Time step used in each numerical simulation was specified as input; careful selection of time step guarantees stable and reliable results, while reducing the computational time. To achieve convergence of solutions of 2D-SWE, the Courant-Friedrich-Lewy (CFL) condition served as a good upper bound estimate for the time step Δt used:

$$\Delta t \leq \frac{\Delta x}{max\left(\sqrt{gH} + \frac{\sqrt{{q_x}^2 + {q_y}^2}}{H}\right)}$$ *Equation 4*

where Δx is the grid size and all other symbols defined in the previous page. However, since q_x, q_y and H are the outcomes of the numerical simulation itself, their maximum values were not usually available prior to the numerical simulation. Therefore, Δt was often estimated from previous experience; for the rainfall intensities, gradient of slope and size of domain used in this project, Δt of 0.005s would normally suffice for Δx of 0.01m.

The grid size Δx was also specified in input; aside from its effect on Δt, it was shown to have negligible effect on the difference in times of concentration predicted.

3.4 Computational parameters

Apart from the correction factor β, time step Δt and grid size Δx, the following parameters were set as input variables in the numerical simulations:

1. Rainfall intensity in metres per second over the duration of simulation.
2. Size and topography of the domain.
3. Distribution and arrangement of any obstacle such as buildings and walls.

It is also necessary to determine the boundary conditions such that all rainfall runoff will only leave the domain at the downstream edge.

3.5 Method of representing buildings and obstacles

There are few different approaches for representing the buildings and obstacles in the numerical model; the building-hole (BH) method and the building-block (BB) method were devised and tested by Schubert et al. (2008) and Cea et al. (2009) in separate occasions. A brief discussion on each method is outlined below.

In the BH approach, any area occupied by the obstacles is left out in the numerical simulations in the rainfall. Therefore, the rainfall intensity would have to be artificially increased uniformly across the remaining area of the domain so that total volumetric rainfall rate remains constant. At the same time, the elevations of these obstacles are raised much higher to ensure that no runoff flows into these ‘holes’. Despite these non-realistic simplification, the BH method produced hydrographs similar to the results from laboratory experiments (Cea et al, 2009).

The BB method resembles the actual physical process of rainfall; the shapes of these obstacles are treated as part of the topography of the domain. Rainfall is applied throughout the domain, including the area occupied by the obstacles. To obtain satisfactory results, this method requires mesh refinement at obstacles to produce good representative of the shapes of these obstacles. This disadvantage causes the BB method to be numerically less efficient than BH, with minimal improvement on the hydrograph predictions (Cea et al, 2009).

From these results, it was decided that for this project, the BH approach would be used owing to its simplicity and efficiency.

3.6 Pre-simulation processing methods

A standardised input data file compatible to the programme written by Liang et al. (2006) was required for each computational simulation. Specifically, the topography of the domain is inputted by specifying the elevation at each grid point; the programme was only capable of reading square mesh grid with whole number co-ordinates. However, some topographies of laboratory experiments were available in the form of unstructured grid, such as that shown in Figure 5. Therefore, to convert the unstructured grid into a square grid (shown in Figure 6), a Matlab script was written to interpolate the elevation linearly at each point of interest. When interpolation was not possible at some grid points, those were the locations of the buildings; using BH method, the elevation of those points was set to 0.1 metres. Finally, an additional runoff leeway with much steeper slope was added further downstream in each domain; this feature prevented the boundary effect to affect the final hydrograph of the numerical simulation. All these features can be visualised in Figure 7.

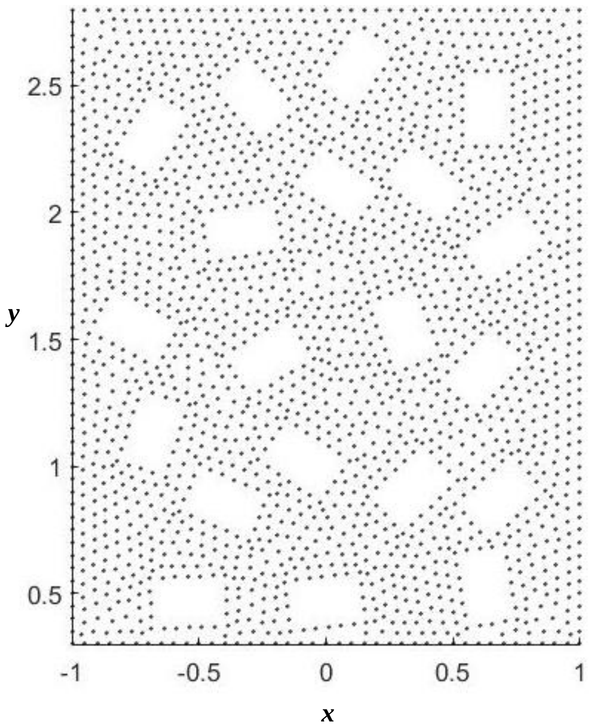

Figure 5: Unstructured grid

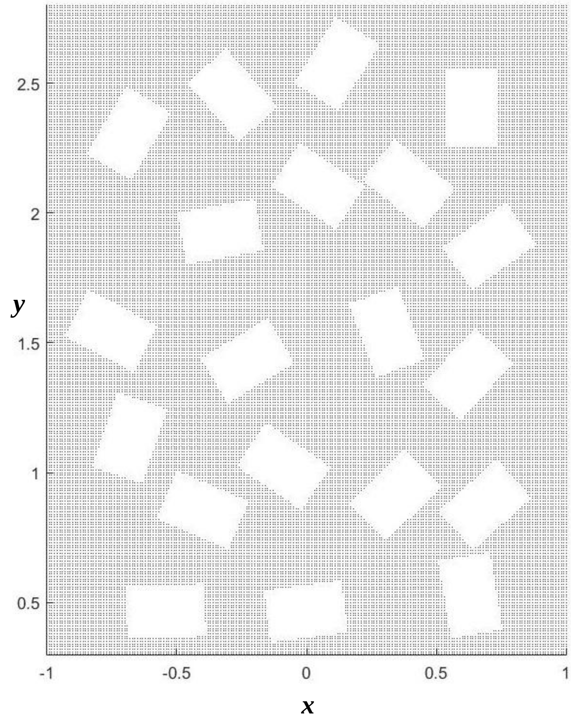

Figure 6: Dense square grid

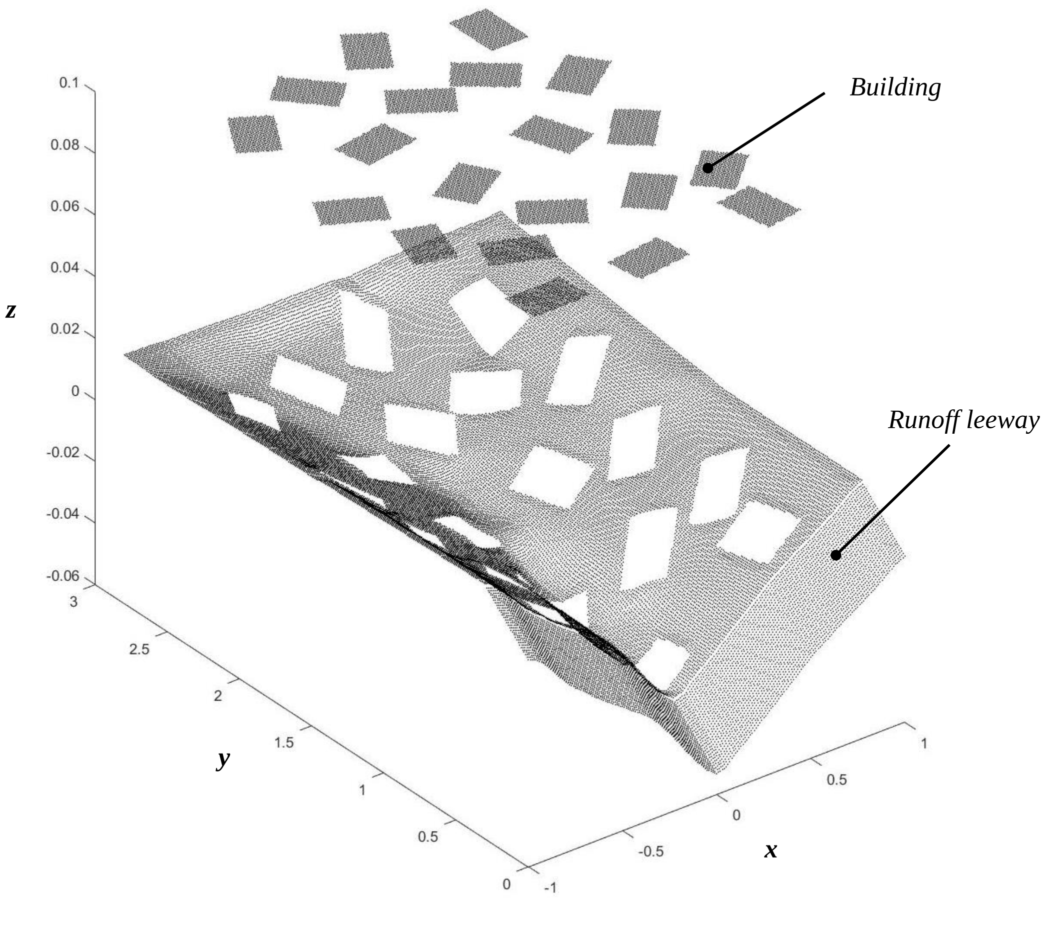

Figure 7: Visualisation of input topography including runoff leeway (BH method)

In subsequent parametric study, a Matlab script was available to generate data of suitable format for regular, staggered and random building matrices on a unidirectional slope (shown previously in Figure 2 in Chapter 1). The script was designed to allow easy alteration of total number of square buildings on the domain and their sizes (Lam, 2016).

3.7 Post-simulation processing methods

Numerical solutions specifying η, q_x and q_y at each grid point at each time step were outputted into a format compatible to Tecplot. The latter is then used to visualise the water depth and its transition in time throughout the whole domain. To obtain the runoff hydrograph of the actual domain, the volumetric rate of outflow at each time step was obtained by integrating q_x along the downstream edge of the main domain, before the water flows to the artificial leeway.

4. Model Improvement and Verification

4.1 Implications from wide channel flow theory

From Chapter 2, it was clear that estimating Chezy coefficient C in the 2D SWE using Manning formula would not be suitable if the bulk of the flow was in laminar region. Hence, to account for the flow of both small and large Reynold-number, another numerical model for calculating C will have to be used. As flow behaves differently in laminar and turbulent regime, it is sensible to divide the analysis into three zones: both laminar and turbulent regimes, and a critical regime in between. Such division is analogous to the Moody Chart for circular pipe flow, which is shown in Figure 8. However, to apply Moody type diagram for wide, open channels, modifications would have to be made based on the original Moody Chart, which is discussed thoroughly below.

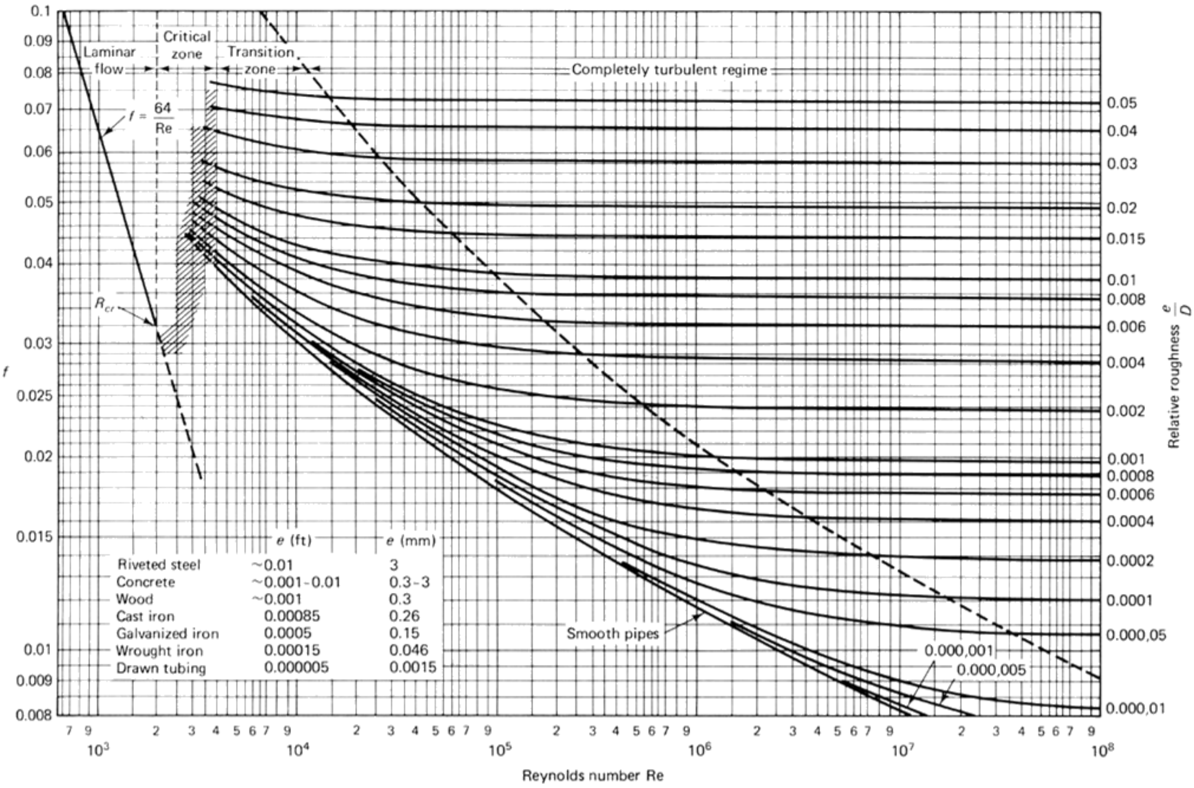

Figure 8: Moody diagram for circular pipe flow

In the laminar flow region ($Re < 2000$), the Hagen-Poiseuille equation can be derived analytically to describe the relationship between resistance coefficient f and Reynolds number of the flow Re. While this is commonly applied to pipe flow, similar derivations can lead to the following expression for infinitely wide channel flow:

$$f = \frac{96}{Re} \text{ (wide channel)}$$

compared to $$f = \frac{64}{Re} \text{ (circular pipe)}$$

The complete derivation is attached in Appendix 1. To arrive at this expression, it is assumed that the fluid is incompressible and Newtonian, i.e. the viscous stresses due to flow are directly proportional to the local strain rate; water is nearly incompressible and Newtonian. It also assumes that the flow is steady and fully developed; while this is generally not true at the beginning of the rainfall when the outflow starts to develop, the equation above still gives a satisfactory estimate of f when the time step used is small. This can be explained by the fact that the change of Re between two time steps is very small compared to Re itself, hence a quasi-steady assumption could be applied in such time-marching numerical analysis.

In the turbulent regime ($Re > 4000$), Colebrook-White formula is commonly used to estimate f in circular pipe. Similarly, a Colebrook-White type formula is often used for open channels with rigid impervious boundary, which takes the form:

$$\frac{1}{\sqrt{f}} = -K_1 log\left(\frac{k_s}{K_2 R_H} + \frac{K_3}{Re\sqrt{f}}\right)$$

where k_s is the equivalent roughness height described in Chapter 2; R_H is the hydraulic radius, $R_H = R$, radius of pipe for circular pipe flow and $R_H \cong H$, water depth for wide channel flow. A spread of values for the constants K_1, K_2 and K_3 for open channel were reported, tabulated below in Table 1.

Channel geometry	Reference	K_1	K_2	K_3	Remarks
Full circular pipe	Colebrook (1939)	2.0	14.83	2.52	
Wide channel	Keulegan (1938)	2.03	11.09	3.41	
Wide channel	Rouse (1946, p. 214)	2.03	10.95	1.70	
Wide channel	Thijsse (1949)	2.03	12.2	3.033	
Wide channel	Sayre and Albertson (1961)	2.14	8.888	7.17	
Wide channel	Henderson (1966)	2.0	12.0	2.5	
Wide channel	Graf (1971, p. 305)	2.0	12.9	2.77	
Wide channel	Reinius (1961)	2.0	12.4	3.4	
Rectangular	Reinius (1961)	2.0	14.4	2.9	Width/depth=4
Rectangular	Reinius (1961)	2.0	14.8	2.8	Width/depth=2
Rectangular	Zegzhda (1938)	2.0	11.55	0	Dense sand

Table 1: Values of constants for Colebrook-White type formula (Yen, 1991)

Taking reasonable median values, the following constants were chosen in the subsequent numerical simulations for simplicity of the Fortran subroutine code (attached in Appendix 2):

$$K_1 = 2.03 \qquad K_2 = 12.0 \qquad K_3 = 2.46$$

For the critical flow regime ($2000 < Re < 4000$), there was no definitive relationship between f and Re in both pipe and wide channel flow. For the sake of numerical analysis, it has been decided that linear interpolation will be used.

Therefore, combining analysis of all regimes yield the following Moody type chart (Figure 9):

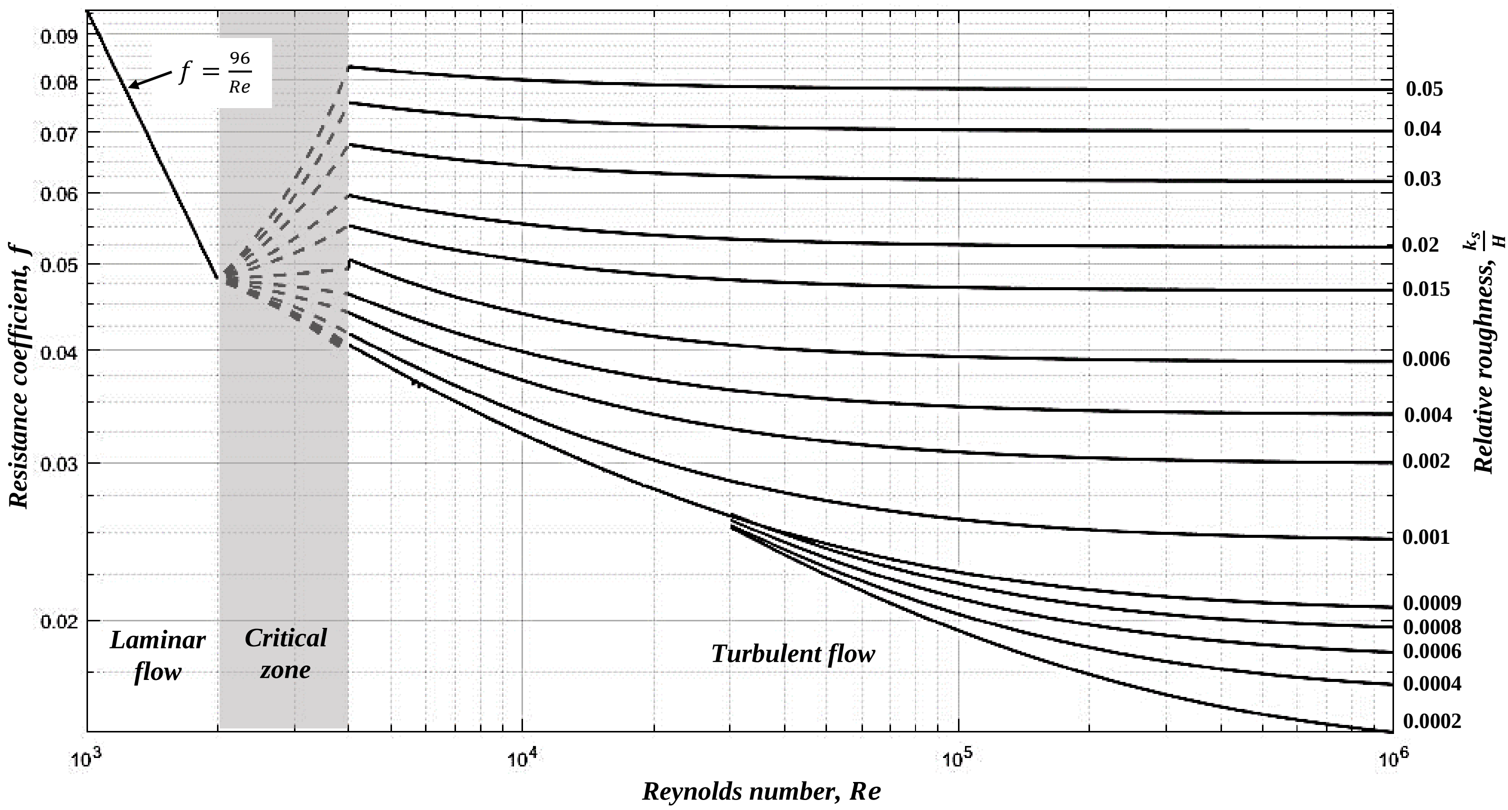

Figure 9: Moody type diagram for wide open channel flow

Once a value of f could be found for any Re, the last step is to convert it to the Chezy coefficient, C for subsequent calculation in 2D-SWE. From the bed shear stress τ_b, one can infer that:

$$\tau_b = \frac{f}{8}\rho U^2 = \frac{g}{C^2}\rho U^2$$

$$C = \sqrt{\frac{8g}{f}}$$

Setting $g = 10\ m/s^2$, the final equations that would be implemented into the programme are:

$$C\left(\frac{k_s}{H}, Re\right) = \begin{cases} \sqrt{\frac{5}{6}Re}, \quad Re < 2000 \\ 50\sqrt{\frac{2}{3}} + \left(\frac{Re - 2000}{2000}\right)\left(C(Re = 4000) - 50\sqrt{\frac{2}{3}}\right), \quad 2000 < Re < 4000 \\ -18\log_{10}\left(\frac{1}{12}\frac{k_s}{H} + \frac{5C}{18Re}\right), \quad Re > 4000 \end{cases}$$

4.2 Implementation into code

The excerpt of the Fortran code pertaining this section is attached in Appendix 3. Notably, there were two challenges in implementing this scheme into the programme:

1. The Colebrook White type formula for turbulent regime is implicit

To solve for C, it would require iteration. An initial value C_0 is obtained to initiate the iteration, using:

$$C_0 = -18\log_{10}\left(\frac{1}{12}\frac{k_s}{H}\right)$$

Subsequently, value of C is iterated in the actual equation until it converges to a value which its difference from the previous iterated value is less than 0.5 (i.e. $\|C_n - C_{n-1}\| < 0.5$). This bound was chosen taking into consideration that typical C values at turbulent regime are greater than 30 $m^{1/2}/s$ if relative roughness height is more than 0.05 (shown in Figure 11), which translates to a maximum percentage error of 1.7% in the estimated C value due to truncation. In exchange, it results in lower computational requirement.

2. C is zero when there is no flow ($Re = 0$)

Although physically true, it possesses problems to the numerical analysis as C is a term in the denominators of the 2D SWE momentum conservation equations. To resolve this issue, a minimum value was imposed, such that:

$$\min(Re) = 0.1, \quad \min(C) = 0.289$$

Hence, the numerical estimates of C have the relationship with Re and k_s shown in Figure 10 and 11.

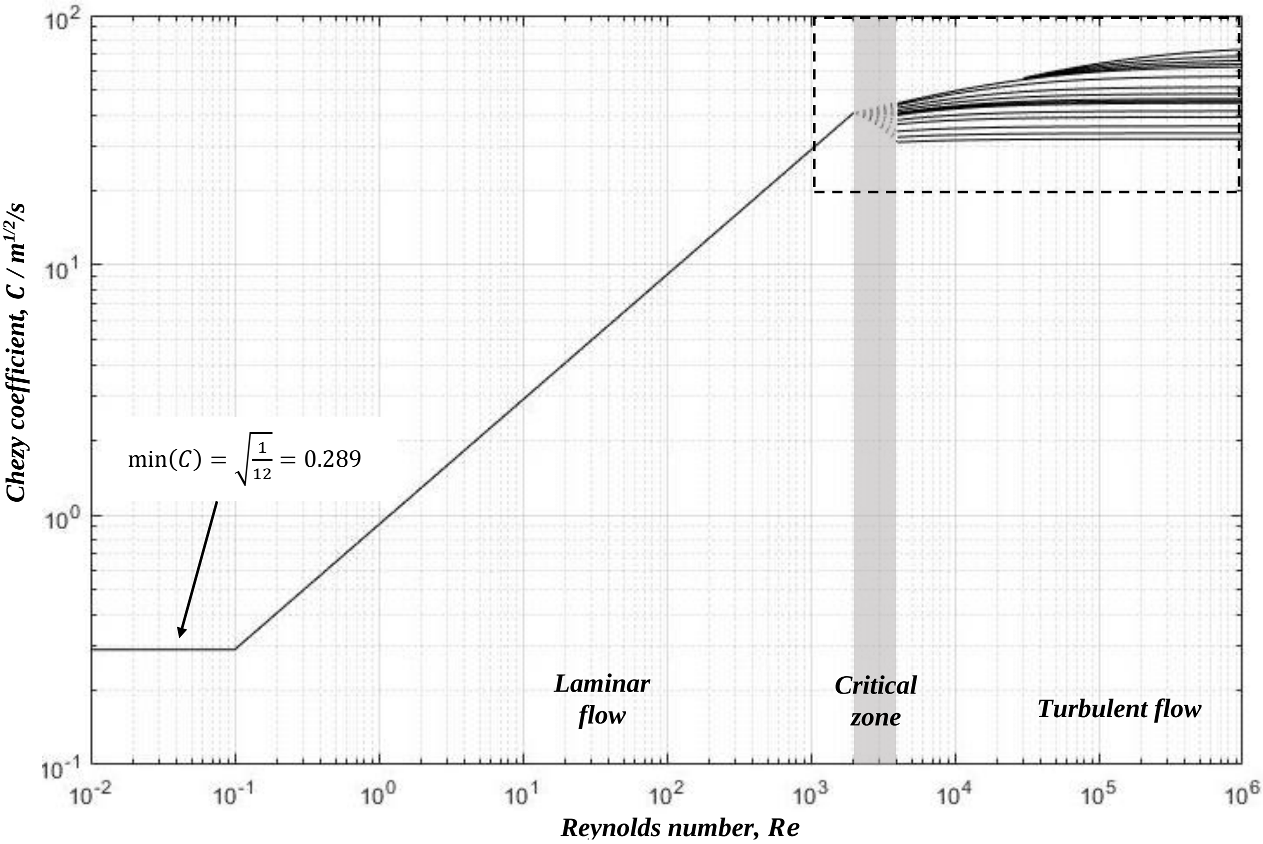

Figure 10: Relationship between C and Re for relative roughness $\frac{k_s}{H}$ between 0.0002 and 0.05

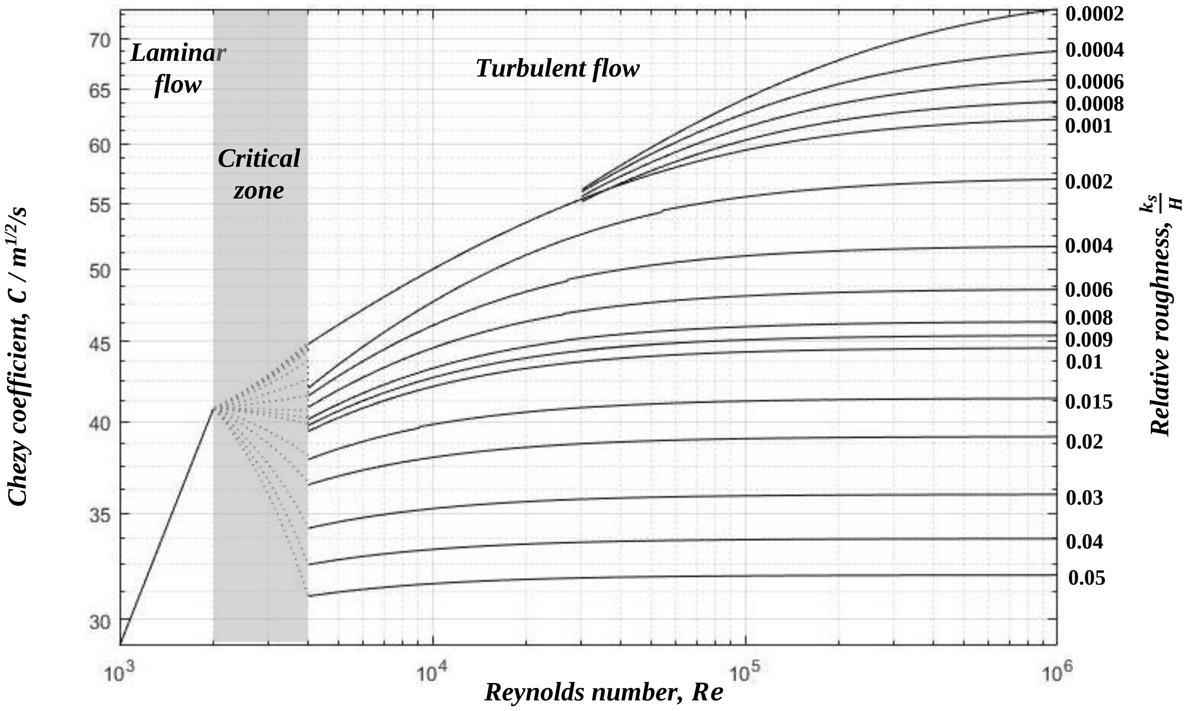

Figure 11: Enlarged region of Figure 10 (in dashed box)

4.3 Model Validation

Following the implementation into codes, it is paramount to investigate the reliability of the proposed method (called k_s-method from this point forward) in modelling urban rainfall numerically. This is achieved by comparing the results of its simulation to both the results from laboratory experiments and from numerical analysis using the traditional Manning method.

In the subsequent sections, physical experiments from Iwagaki (1955), Cea et al. (2008) and Cea et al. (2009) were chosen, which amounts to more than 50 sets of data to compared with.

4.3.1 1D model validation: Iwagaki (1955)

Iwagaki's experiments involved a 24 metre laboratory flume made of smooth aluminium divided into three different slopes, as shown in Figure 12. From upstream to downstream, the slope of the flume ($\sin\theta$) reduced from 0.020, 0.015 to 0.010 at 8 metre interval, forming two kinks at $x = 8\ m$ and $16\ m$ points. Uniform rainfall of 3890, 2300 and 2880 mm/h was applied to the three sections respectively from upstream to downstream, as shown in Figure 13. Three different durations of rainfall were applied to the flume to create three experimental cases: they were 10, 20 and 30 seconds, which are denoted as Case I, Case II and Case III.

To simulate Iwagaki's experiments numerically, the mesh size is chosen to be $\Delta x = 0.25\ m$, which creates 96 elements along the flume, and an additional 30 elements were added for creating a steep runoff leeway for the purpose described in Chapter 3.6. To satisfy the CFL condition mentioned in Chapter 3.3, a minimum recommended time step is 0.125 s. Hence, Δt was chosen to be 0.05 s.

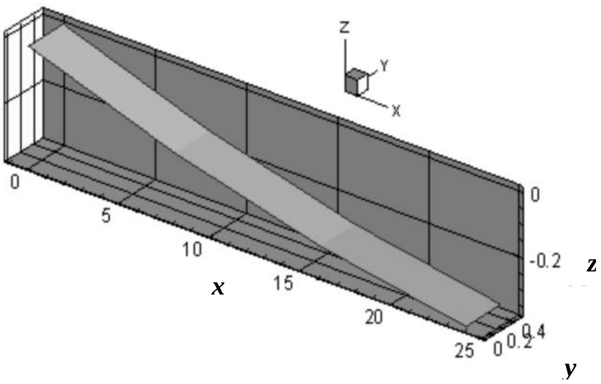

Figure 12: Iwagaki's three-slope flume in 3D-space (Chan, 2012)

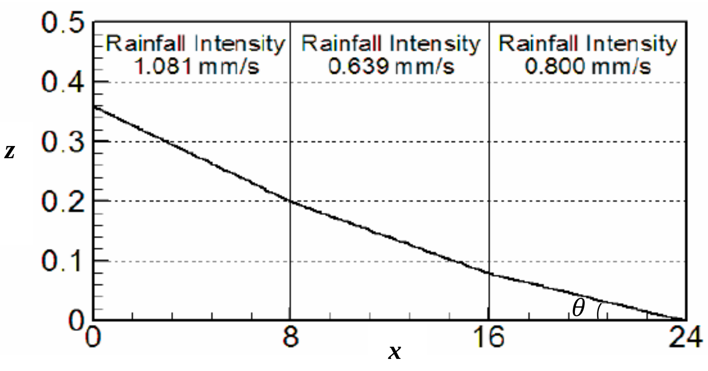

Figure 13: Rainfall intensity (mm/s) in each slope (Cea et al. 2008)

First, a consistent value of k_s to describe the roughness of the flume is required to evaluate the reliability of the k_s-method. Therefore, the experiment with 30 seconds rainfall (Case III) was chosen to calibrate the value of k_s; it was found that $k_s = 0.6\ mm$ gives the best prediction of the peak outflow, and fits the experimental data curve reasonably well (Figure 14). Given that a typical aluminium surface would be expected to have k_s of an order of magnitude smaller, the larger effective k_s in this experiment could be due to accumulation of dust on the surface or a much poorer workmanship. Nonetheless, the results from numerical analysis correctly pointed out that the smoother the surface (i.e. lower k_s), the quicker the outflow reaches its peak and the sharper the peak. This can also be observed in Figure 15 and 16 respectively.

A sensitivity analysis was also performed to study the effect of varying k_s to the predicted peak outflow and time when this happened. Further investigation suggested that both factors were very sensitive to value of k_s, and became even more so when k_s reduces (Figure 15 and 16). This observation indicates the higher likelihood of uncertainty and error in numerical prediction of hydrograph features in smoother surface.

A similar process was used to calibrate the Manning coefficient n; the optimal n was found to be around 0.011 s/m$^{1/3}$ (Figure 17) As comparison, Cea et al. (2008) calibrated n against Case I and obtained a comparable value of 0.009 s/m$^{1/3}$. Furthermore, Chan (2012) noted that a n value larger than 0.009 s/m$^{1/3}$ can be used to better fit the results.

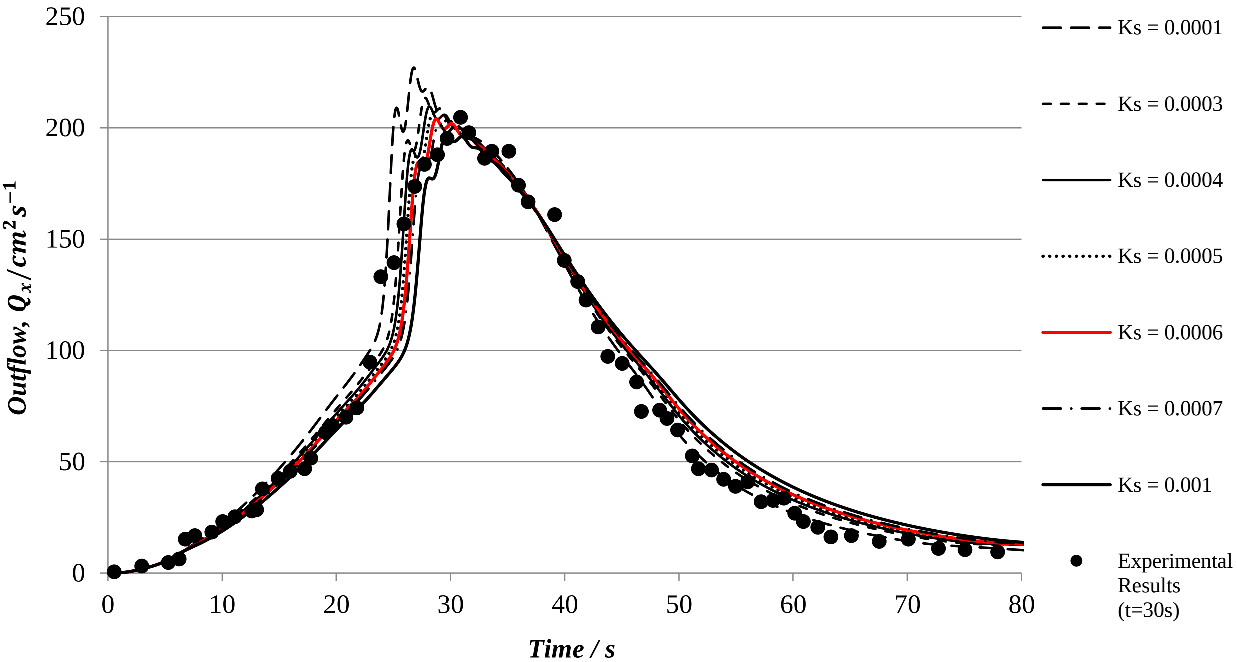

Figure 14: Sensitivity of the numerical results to k_s(in metres) in Iwagaki's experiment (Case III)

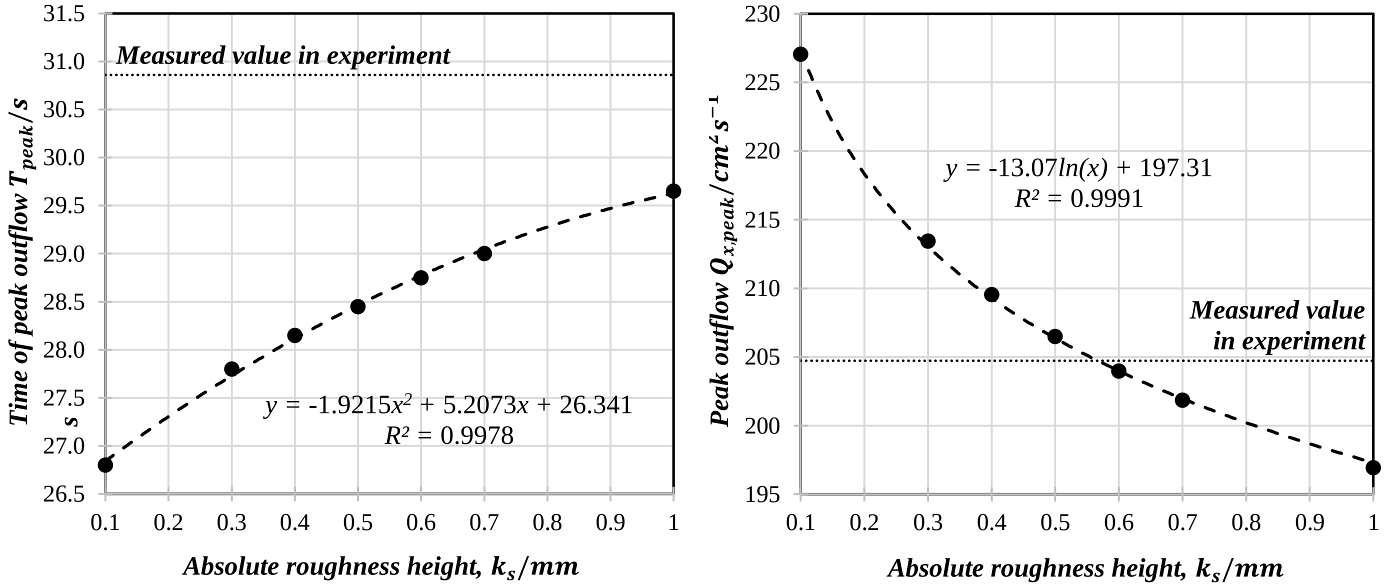

Figure 15 and 16: Sensitivity of the numerical results to k_s in terms of peak outflow and its time

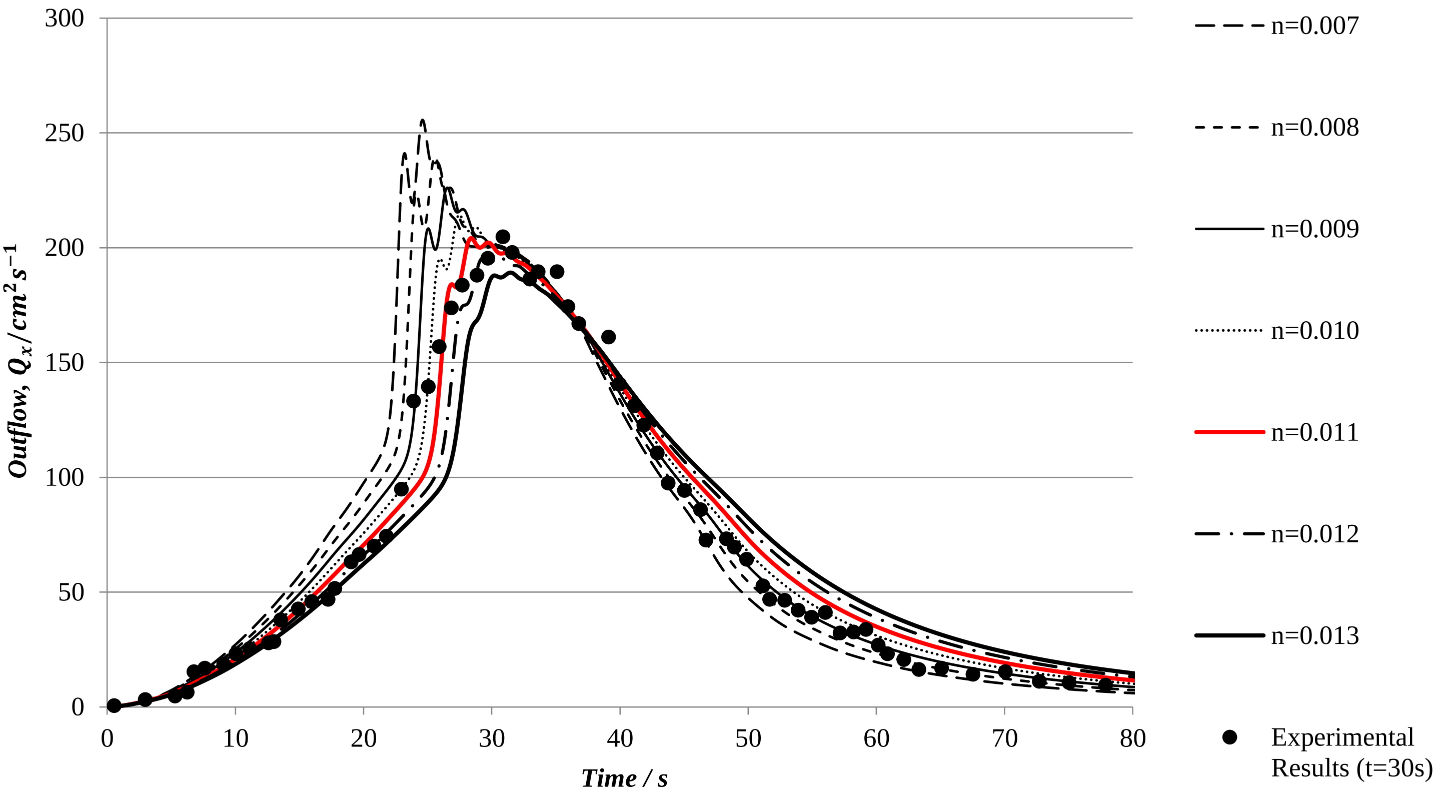

Figure 17: Sensitivity of the numerical results to n (in s/m$^{1/3}$) in Iwagaki's experiment (Case III)

Using $k_s = 0.6\ mm$ and $n = 0.011\ s/m^{\frac{1}{3}}$, numerical analysis was performed for the other two cases. Figure 18 below and Table 2 overleaf summarise the key results.

From the results, it was clear that the hydrographs predicted from k_s-method was almost identical to that from the Manning method particularly for those cases with higher general flow Q_x. Bearing in mind that Manning method assumes turbulent flows (Chapter 2), this seems to suggest that bulk of the flow was in turbulent regime in these experiments, and the two methods converged to the same hydrographs as rainfall was of longer duration which caused greater outflow. This was supported by the fact that critical regime will be reached when $Q_x > 6.5\ cm^2s^{-1}$ at any point along the flume (derived below), which was only 9%, 5% and 3% of $Q_{x,peak}$ of respective cases. Note that for rectangular ducts, the characteristical dimension in Reynolds number is the hydraulic diameter, taken as 4 times the flow depth:

$$Re = \frac{4U_xH}{kinematic\ viscousity} = \frac{4Q_x}{1.3 \times 10^{-6}} > 2000$$

Both methods predicted the shape of laboratory hydrograph satisfactory for all three cases. Other than the noticeable time lag in Case 1 and the higher peak outflow prediction in Case 2, the percentage error of other predictions of $Q_{x,peak}$ and T_{peak} were less than 8%. In fact, the two anomalies were noted previously in theoretical analysis completed by earlier research (Iwagaki, 1955). It was therefore unlikely that the anomalies were attributed to any error in the numerical simulation itself.

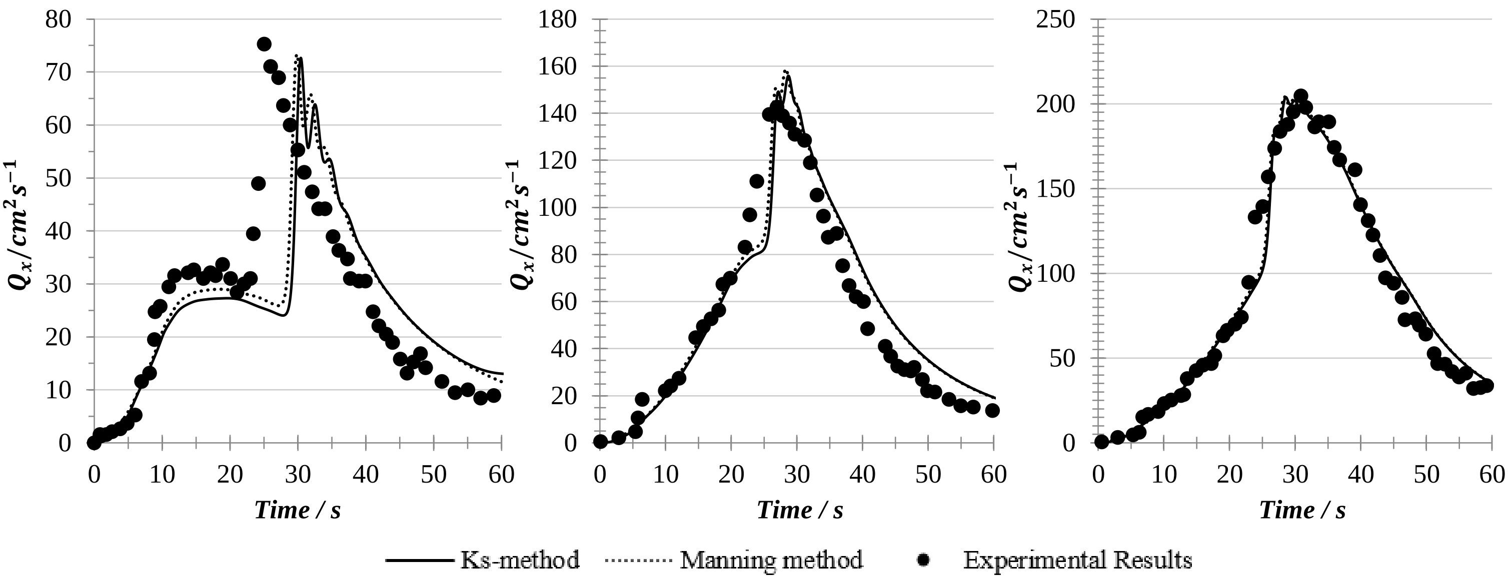

Figure 18: Numerical and experimental hydrograph for the 1D model validation test. Case 1 (left), Case 2 (middle) and Case 3 (right)

	Case 1			Case 2			Case 3		
Method	**Lab**	k_s	n	**Lab**	k_s	n	**Lab**	k_s	n
$Q_{x,peak}$ $/cm^2s^{-1}$	75.26	72.67	73.30	142.63	155.94	158.67	204.74	204.00	204.13
T_{peak}/s	25.05	30.45	29.85	26.95	28.70	28.35	30.86	28.60	28.40

Table 2: Peak discharges $Q_{x,peak}$ and the time these happened T_{peak} for all cases

4.3.2 2D model validation: Cea et al. (2008)

In the laboratory experiment, three planes of stainless steel were inclined inwards at a slope of 0.05, such that they formed a valley in the middle of the flume (Figure 19). Two impermeable walls were placed on the two side planes to stop the upstream runoff from directly entering into the trough of the valley. This delayed the time when peak outflow occurred. The dimensions of the basin is $2m \times 2.5m$, with the longer side parallel to the direction of valley.

Three rainfall cases were applied uniformly to the domain by using a grid of 100 nozzles distributed evenly over the basin. Case I involved applying a rainfall intensity of 317 mm/h for 45 seconds, and no rainfall thereafter. Case II was a two-stage rainfall process in which 320 mm/h of rainfall intensity was applied at two 25-second intervals, with a 4 second pause in between the two intervals. Case III was similar to Case II except that the rainfall intensity was 328 mm/h and the pausing time was 7 seconds (Figure 21).

To numerically simulate these cases, the BH method was chosen and a mesh size $\Delta x = 0.01\ m$ was chosen; this was 25 times finer than Δx used in the Iwagaki's experiments. This is because the length scale of this domain was 10 times smaller than of Iwagaki's flume; it was also more than twice as steep, which could produce unphysical fluctuations in numerical analysis if grid was not sufficiently fine. This issue arose as the elevation difference in neighbouring nodes were modelled as steps in the numerical model, whereas the physical surface was smooth.

To satisfy CFL condition in Chapter 3.3, the time step Δt used is 0.005s. Runoff leeway of 30 grid points (equivalent to $0.3m$) and 0.05 slope was added at the downstream, shown in Figure 19, for reason discussed in Chapter 3.6.

Using similar procedure as that in Iwagaki's simulation, k_s was calibrated using Case I. However, unlike Iwagaki's, there were difficulties in comparing the sensitivity of k_s using the

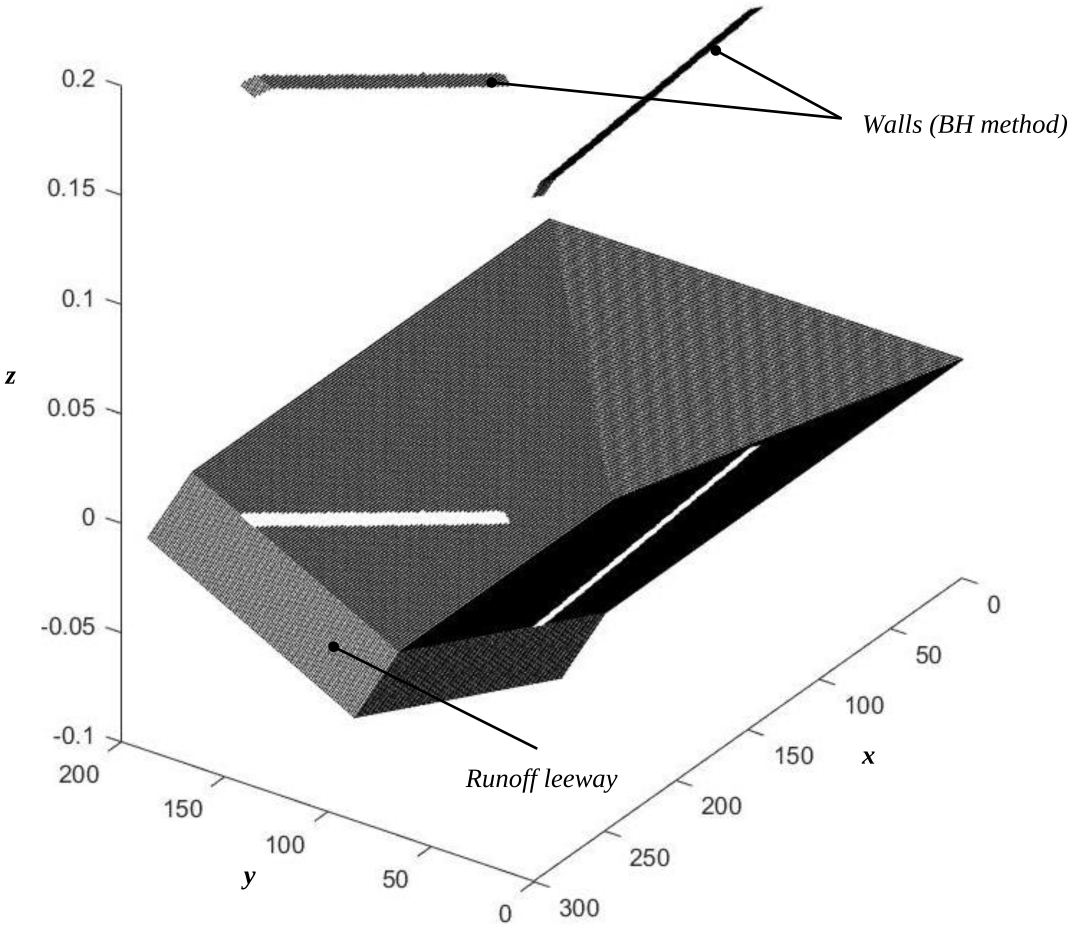

Figure 19: Topography of numerical analysis using BH method and added runoff leeway

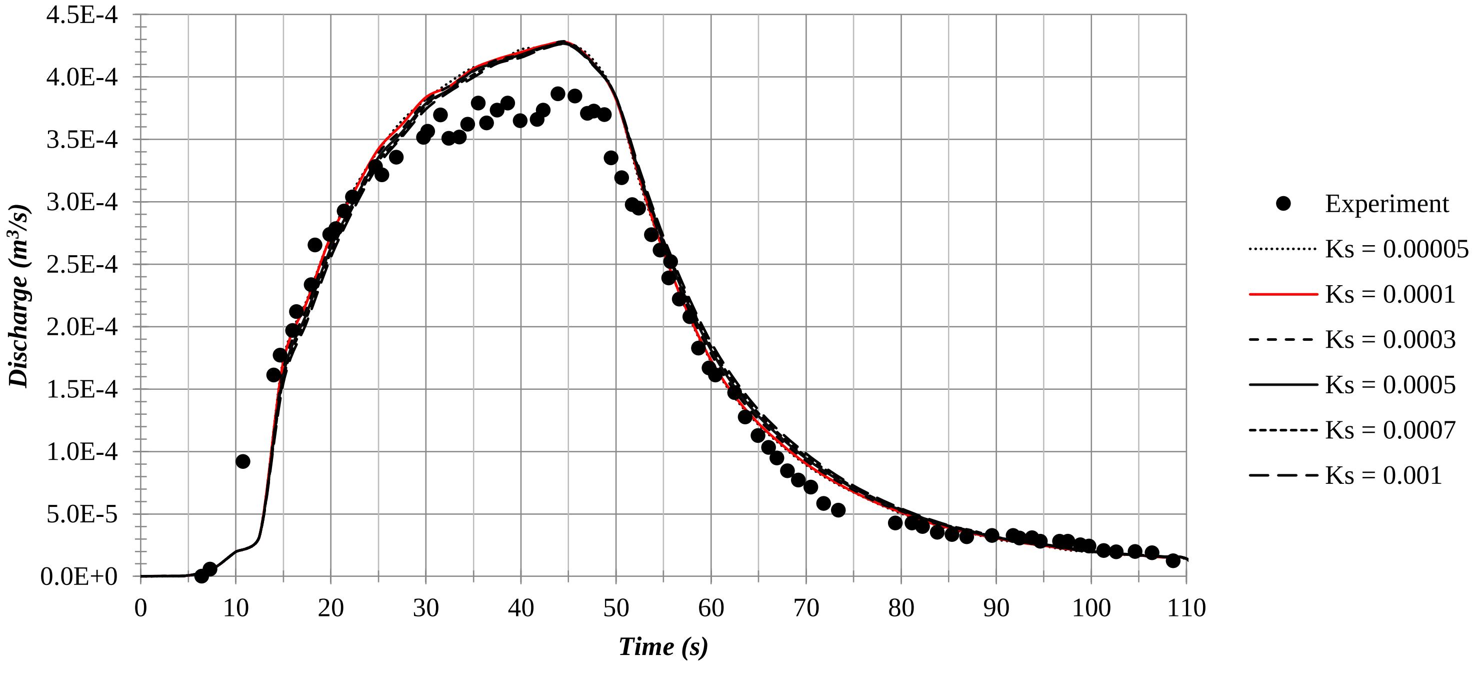

Figure 20: Sensitivity of the numerical results to k_s (in metre) in Cea's 2008 experiment (Case I)

peak discharge rate and time as the occurrence of the peak of hydrographs were close to identical; the main differences in hydrographs arose from the gradients of the rising and falling limbs, as shown in Figure 20; the smaller the value of k_s, the steeper the hydrograph gradient around the peak. Hydrograph of $k_s = 0.1mm$ best matched the experimental data, which was chosen subsequently for modelling Case II and Case III. Nonetheless, the calibration of Manning coefficient n was not needed as previous researchers found that $n = 0.009$ s/m$^{1/3}$ fits the experimental data satisfactorily (Cea, 2008, verified by Chan, 2012). Results of all cases and the contour of typical water depth when it rains were shown in Figure 21.

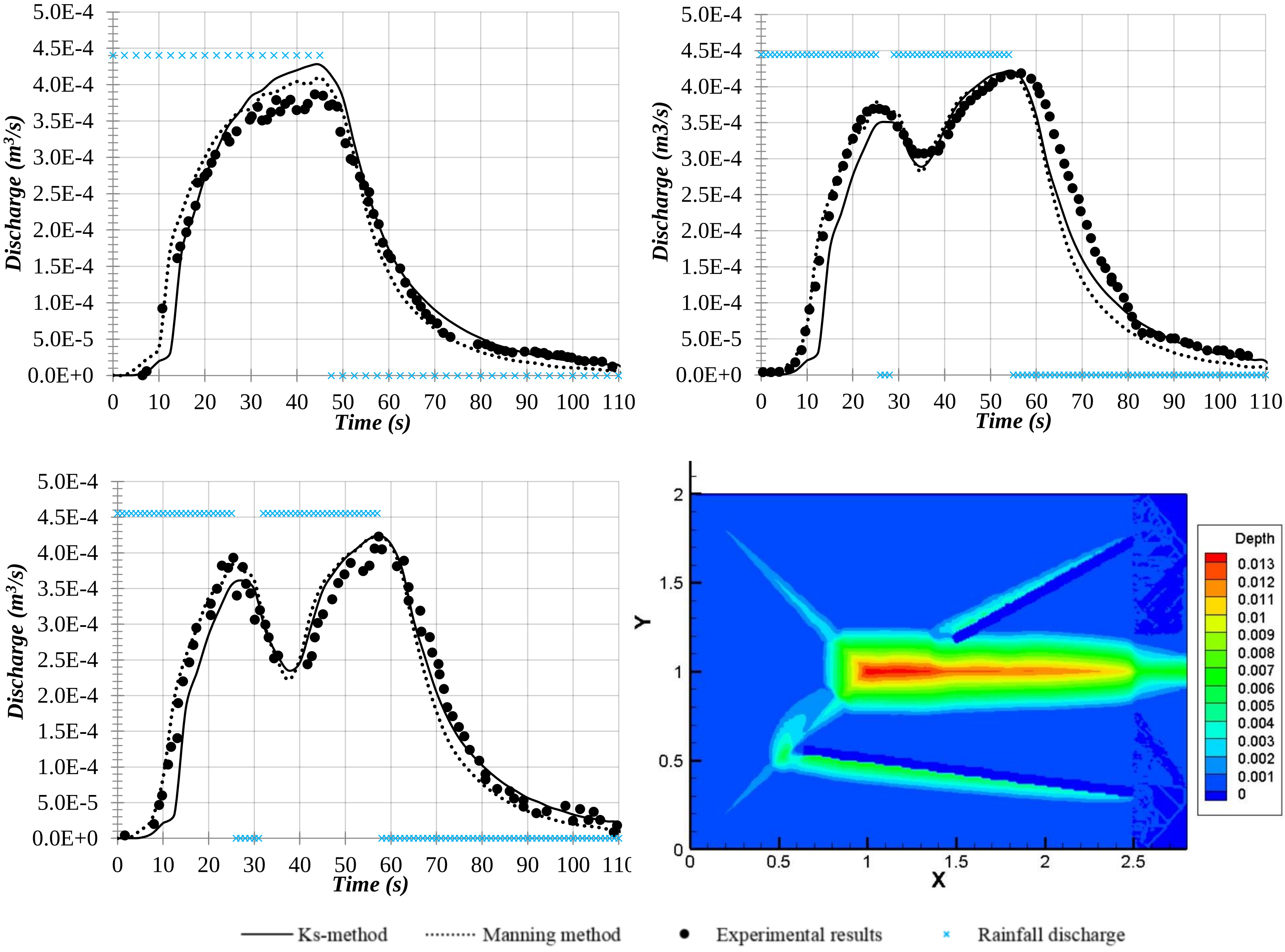

Figure 21: Experimental results and numerical hydrographs: Case I (top left), Case II (top right) and Case III (bottom left), and a typical water depth near the peak outflow (Case I)

	Case I			Case II			Case III		
Method	**Lab**	$\boldsymbol{k_s}$	$\boldsymbol{n}$	**Lab**	$\boldsymbol{k_s}$	$\boldsymbol{n}$	**Lab**	$\boldsymbol{k_s}$	$\boldsymbol{n}$
$\boldsymbol{Q_{x,peak}}$ $\boldsymbol{/cm^3 s^{-1}}$	386.6	427.4	409.7	416.4	421.3	420.0	422.9	424.3	422.4
$\boldsymbol{T_{peak}/s}$	43.9	45.0	45.0	54.5	55.0	55.0	57.3	57.5	57.5

Table 3: Peak discharges $Q_{x,peak}$ and the time these happened T_{peak} for all cases

Overall, all numerical simulations return satisfactory results; they successfully predict the shape of outflow hydrographs, particularly on the prediction of second peak in Case II and Case III: the percentage error in estimations of $Q_{x,peak}$ and T_{peak} were within 2% as compared to the laboratory results.

In Case I, the $Q_{x,peak}$ was slightly overestimated at a percentage error between 5% to 10%. It was suspected that when the tap was first turned on, it took some time for the rainfall intensity to change from zero to a constant value (Cea et al, 2008); total volume of rainwater fell on the board was slightly smaller than expected, causing the experimental hydrograph to be of smaller area and $Q_{x,peak}$ to be generally lower. Although the Manning method appeared to give a better estimate of $Q_{x,peak}$, there was no measure to what extent the effect of initial rainfall issue was, and hence no inference could be drawn on the comparison of the performance of both methods.

In Case II, there was a perfect fit of experimental data to those estimated using Manning method at the first rising limb, despite not taking into account laminar flow regime; prediction of k_s-method was lagging behind by approximately 3 seconds; however, both methods predicted the second rising limb and the subsequent $Q_{x,peak}$ satisfactorily. This puzzling observation could be explained if the Reynolds number threshold set for the laminar-turbulent transition ($2000 < Re < 4000$) in the k_s-method was too high. If transition occurred at smaller flow rate, the Chezy coefficient C could have been higher, which induced higher flow rate earlier. The anomaly at the descending limb could be due to the leakage in nozzles even after the rain was ceased in the laboratory (Cea et al, 2008).

Case III started off similarly as Case II, but unlike Case I, k_s-method appeared to give better prediction past the second peak. However, no inference could be drawn due to the same reason discussed in Case I.

4.3.3 2D model validation: Cea et al. (2009)

The topography of the laboratory experiments was similar to that in 2008: three planes of stainless steel were arranged at slopes of approximately 0.05, forming a rectangular basin of dimension $2m \times 2.5m$ with feature similar to a valley in the middle. However, instead of two walls in 2008, the basin was occupied by 12 or 20 buildings arranged in regular, staggered or random placement. There were a total of 8 different urban geometry configurations tested in this set of experiments (Figure 22). Each building had a rectangular plan of dimension $30cm \times 20cm$, and was $20cm$ tall.

The rainfall was designed to be spatially uniform. This was achieved by placing a grid of 100 nozzles covering the whole basin (Figure 23 and 24). The rainfall discharge rate was set to be 7 litres per minute. By maintaining the rainfall duration at 20, 40 and 60 seconds, 3 sets of hyetographs were produced (Table 4). Such intense but short rainfalls were meant to simulate extreme precipitation events (Cea et al, 2009).

During the experiment, two global uncertainty errors were identified: uncertainty in measurement of outlet discharge and imposed rainfall intensity. It was found that the combined errors were in between 5% to 10%, mainly due to the inaccuracy in the nozzle.

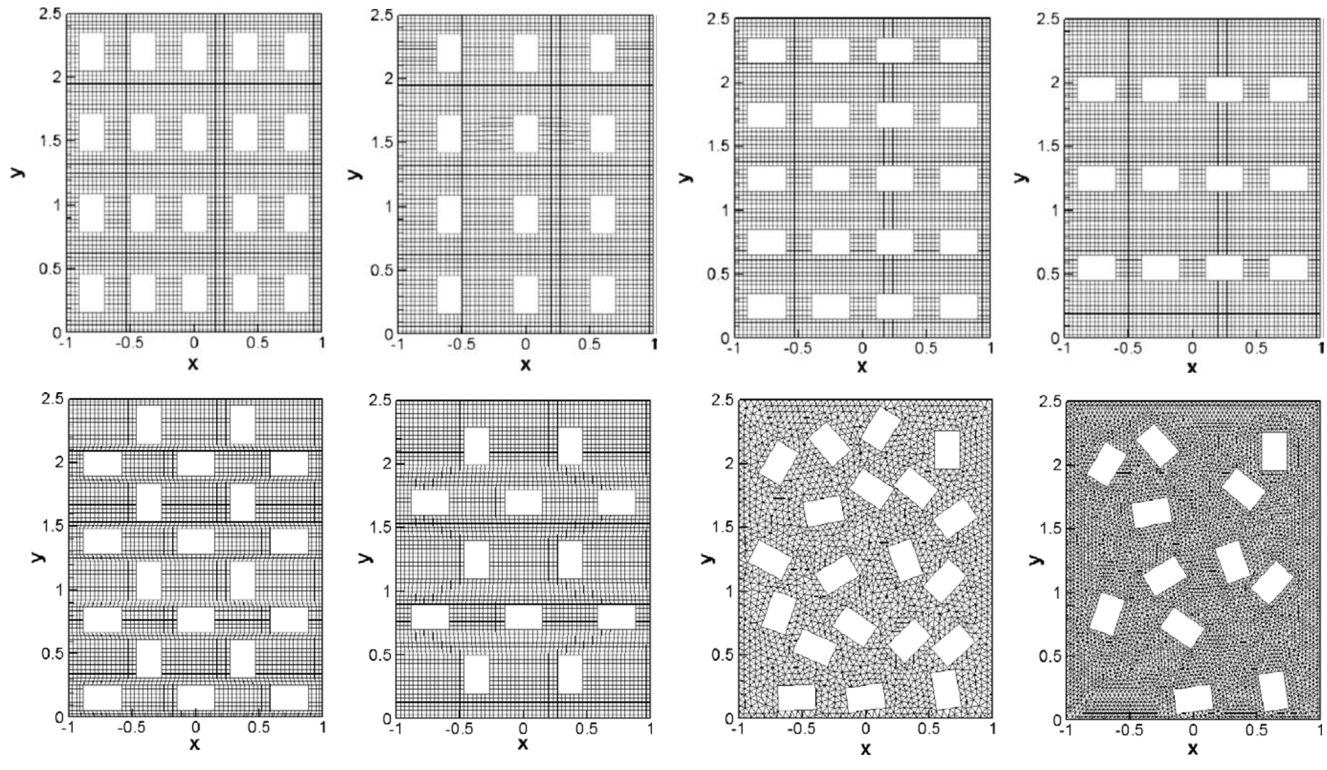

Figure 22: Urban geometry configurations. From top left to top right: Y20, Y12, X20, X12; from bottom left to bottom right: S20, S12, A20 and A12 (Cea et al, 2009)

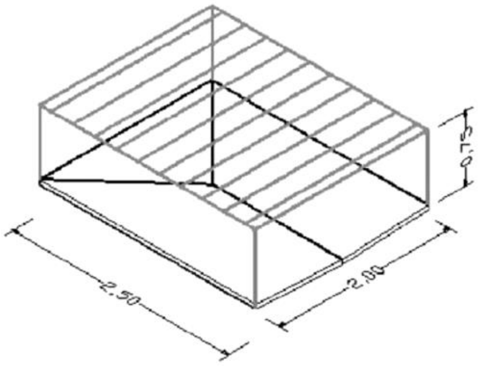

Figure 23: 3D sketch of the rainfall simulator (Cea et al, 2009)

Figure 24: Rainfall simulator with configuration A20 (Cea et al, 2009)

Hyetograph	**Rainfall discharge / l/min**	**Rainfall intensity / mm/h**	**Rainfall duration / s**
Q25T20	25	300	20
Q25T40	25	300	40
Q25T60	25	300	60

Table 4: Hyetographs used in the experiments (Cea et al, 2009)

Given a fixed rainfall intensity, the sensitivity of the outlet hydrograph to the spatial variations of rainfall intensity measured in the experiments was negligible (Cea et al, 2009).

It was also noted that the real topography of the basin was different from the designed topography due to deformations on the three plates. As there was significant difference in the results of numerical simulations for each topography, it became vital to compare the experimental hydrographs with those from the actual deformed topography. To establish this, the basin was filled with different levels of still water, and the wet-dry front position was measured for each case. Therefore, a bed-elevation contour map was obtained (Figure 25); real basin topography was interpolated from the measured contour levels and used in the subsequent numerical simulation.

Since the domain size and slope of topography were similar to previous experiment in 2008, the mesh size and times step used were identical: $0.01\ m$ and 0.005s respectively. Again, a runoff leeway of 30 grid points and slope 0.05 was added. The BH method was adopted when modelling the buildings for reasons stated in Chapter 3.5.

Next, k_s was calibrated using the Y20 configuration with hyetograph Q25T60. Similar to calibration results from Cea et al (2008), varying k_s from the magnitude of micrometre to millimetre has negligible effect on the numerical outlet hydrograph (Figure 26). All hydrographs have similar $Q_{x,peak}$ values that were less than 10% away from the measured experimental value (Table 5); they were in the range of the global uncertainty errors aforementioned. Since none of the k_s values gave significantly superior predictions, k_s was chosen to be $0.05\ mm$ considering that it gave the smallest percentage error in $Q_{x,peak}$ in this test case, while being a commonly used roughness height for steel.

Manning coefficient need not be calibrated as it was previously found that $n = 0.016\ s/m^{\frac{1}{3}}$ was optimal for these sets of experiments (Cea et al, 2009).

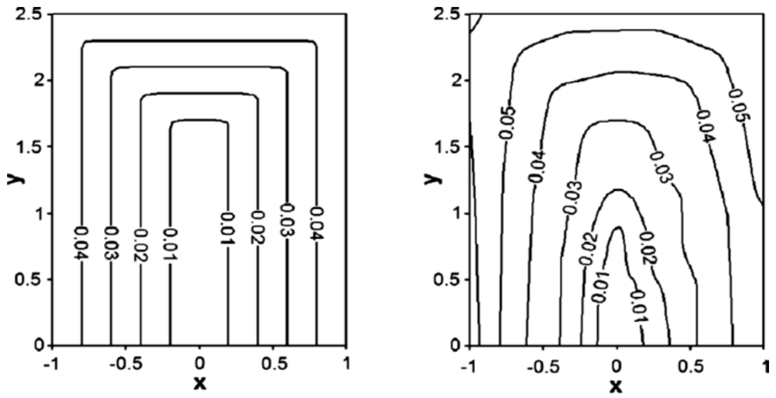

Figure 25: Designed (left) and real (right) basin topography

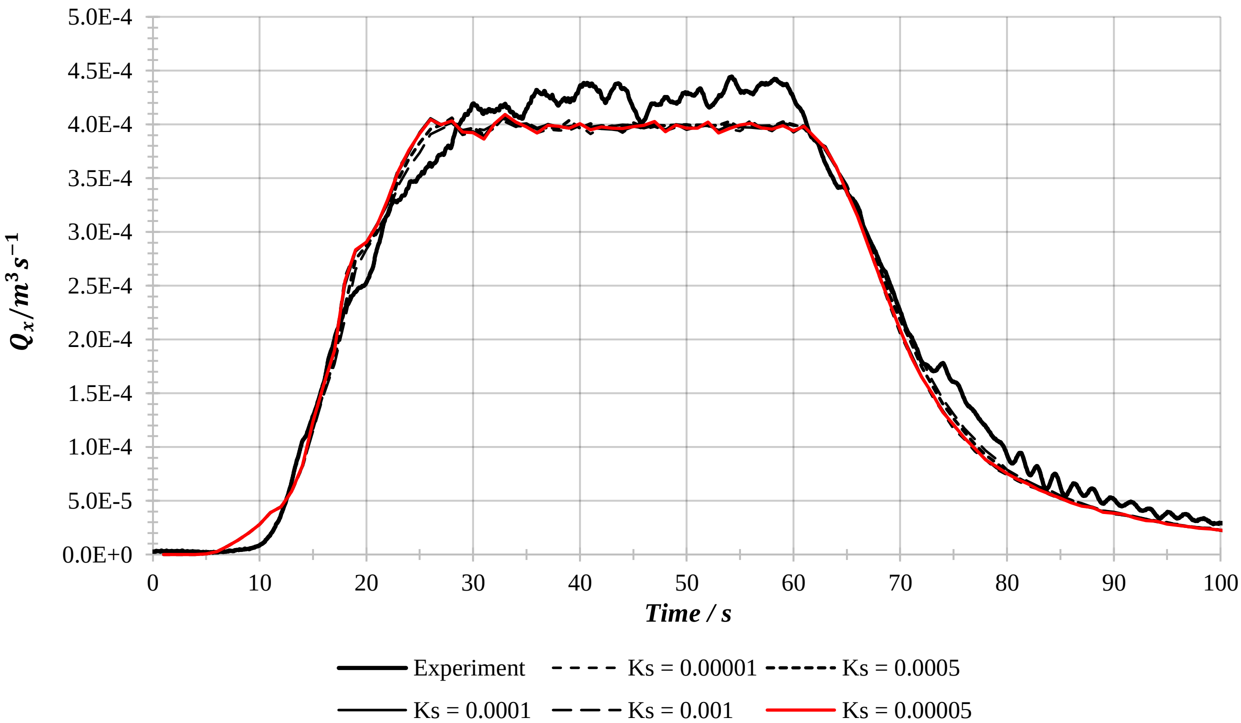

Figure 26: Sensitivity of the numerical results to k_s (in metre) in Cea's 2009 experiment (Y20, Q25T60)

	Lab	k_s/mm				
		0.01	**0.05**	**0.1**	**0.5**	**1**
$Q_{x,peak}/\mathrm{cm^3 s^{-1}}$	444.44	405.02	409.21	405.94	408.27	402.52
Percentage Error	0%	8.9%	7.9%	8.7%	8.1%	9.4%

Table 5: Peak discharges $Q_{x,peak}$ and their percentage errors from the experimental data

Using the calibrated k_s and n values, numerical simulations were performed on all 8 building configurations for all hyetographs stated in Table 4. This gives in total of 24 sets of comparison between experimental data and numerical results from both k_s-method and Manning method (Figure 27, 28, 29 and 30).

Overall, the shape of all numerical hydrographs matched the experimental hydrographs: the onset of outflow discharge, the discharge peak, time when it first reached the peak and subsequent reduction in outflow due to ceasing rainfall were generally predicted by both numerical models. k_s-method consistently produce a sharper peak as compared to Manning method in all cases; this is reasonable considering that a lower value of k_s was used as compared to previous simulations despite a bigger Manning coefficient, which implied that the k_s-method assumed a smoother surface. The experimental results, on the contrary, indicated that the gradients at two sides of the peaks were less steep than what were predicted

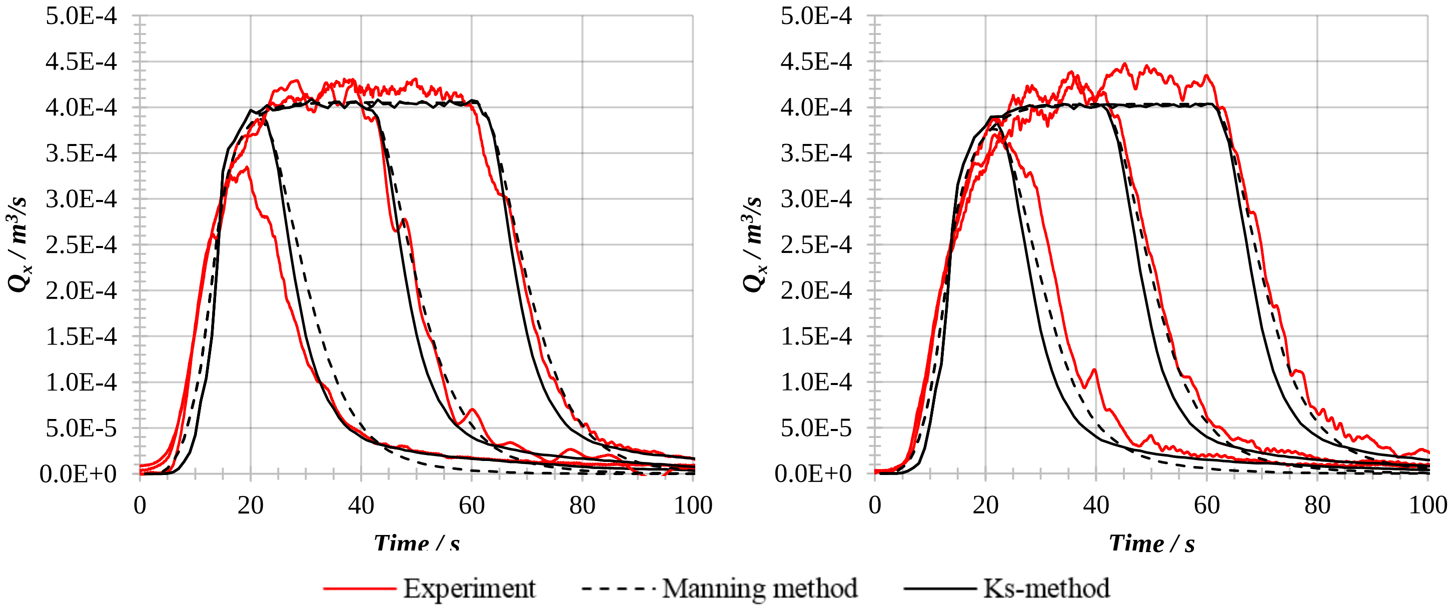

Figure 27: Experimental results and numerical hydrographs for T20, T40 and T60 (left: X12, right: X20)

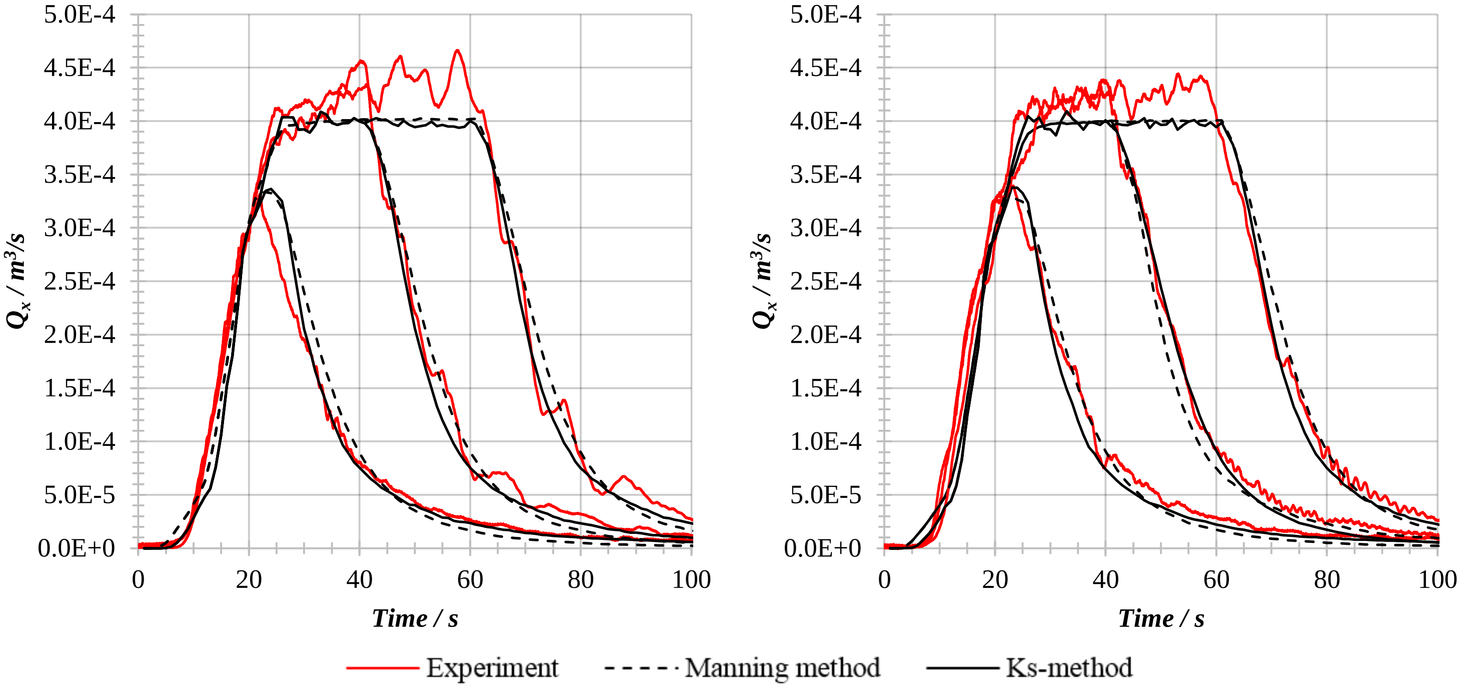

Figure 28: Experimental results and numerical hydrographs for T20, T40 and T60 (left: Y12, right: Y20)

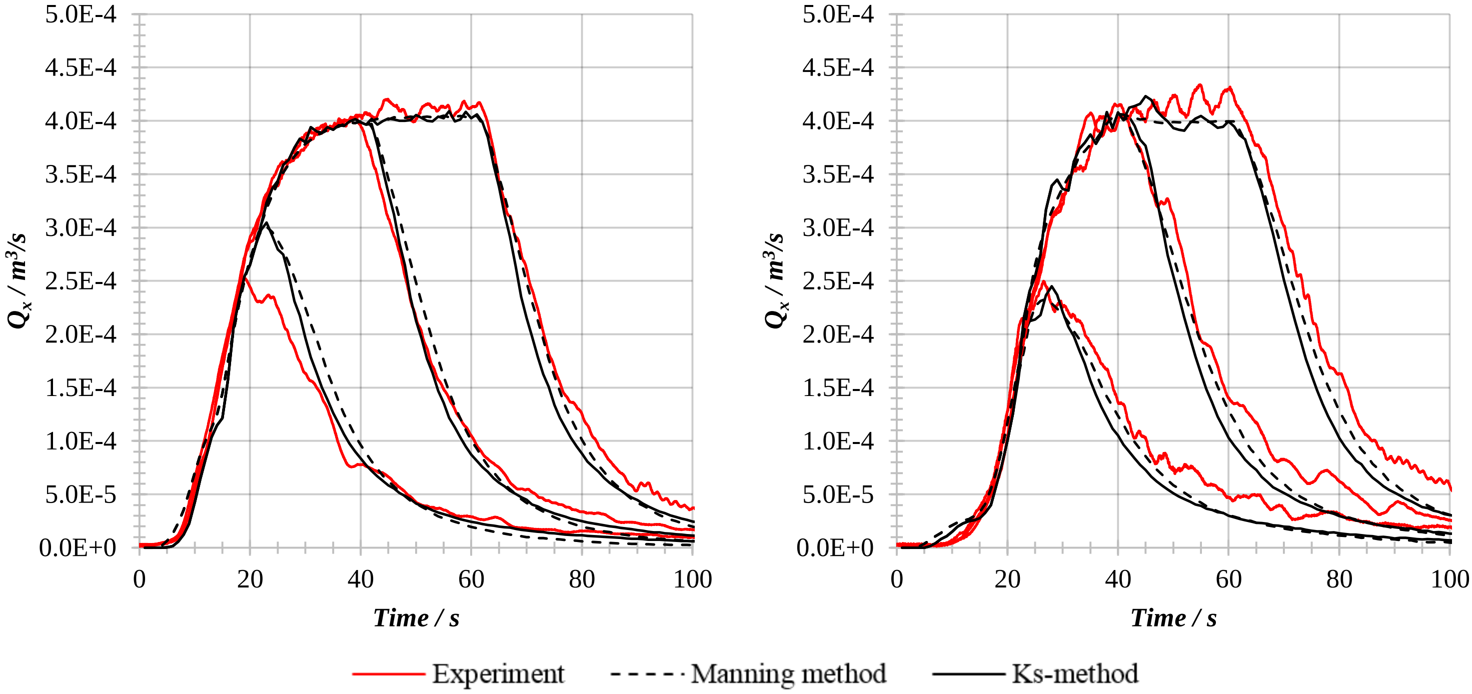

Figure 29: Experimental results and numerical hydrographs for T20, T40 and T60 (left: S12, right: S20)

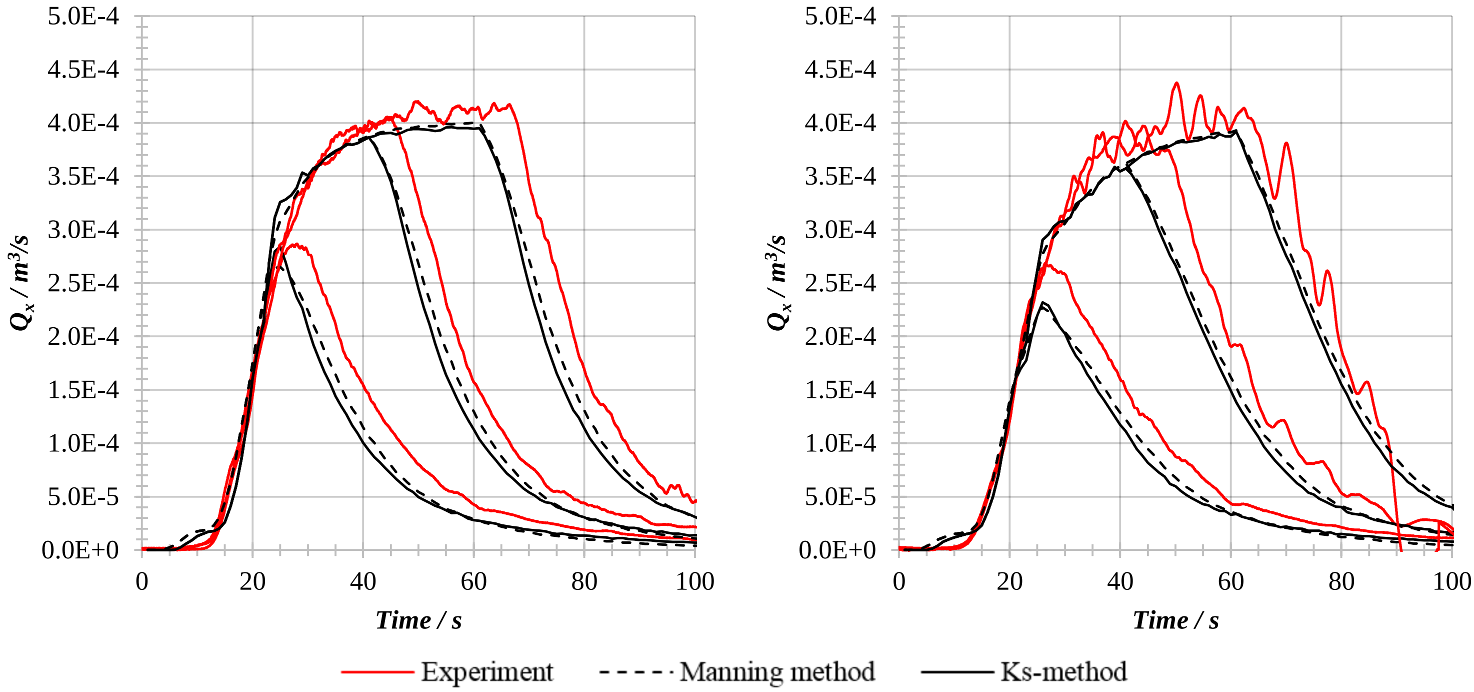

Figure 30: Experimental results and numerical hydrographs for T20, T40 and T60 (left: A12, right: A20)

by the k_s-method. Although a larger k_s value could be used for slightly more optimal estimates, the previous k_s calibration results suggested that the improvement in prediction was insignificant even if k_s was increased to the magnitude of millimetres (Figure 26).

A closer examination of the results were carried out to check the deviation of estimated peak discharges and hydrograph widths using k_s-method as compared to those from experiments and Manning method (Figure 30 and 31). Hydrograph widths are obtained by measuring the duration of which outlet discharge stays above a quarter of its peak. Overall, T40 and T60 numerical simulations were very satisfactory, with almost all points fell within the 10% percentage error threshold; this is consistent with the global uncertainty errors measured. T20 numerical results were poorer as they have higher percentage errors, but the magnitude of these errors remained similar as those from T40 and T60. One plausible explanation was that the dominating experimental uncertainties were absolute and independent of the period of rainfall, such as the leakage of the nozzles once they were turned off.

Although k_s-method predicted larger $Q_{x,peak}$ than those from Manning method, the former still consistently underestimated $Q_{x,peak}$ for the laboratory experiments T40 and T60 (Figure 30). This was not surprising considering that the rainfall discharge could have small variation

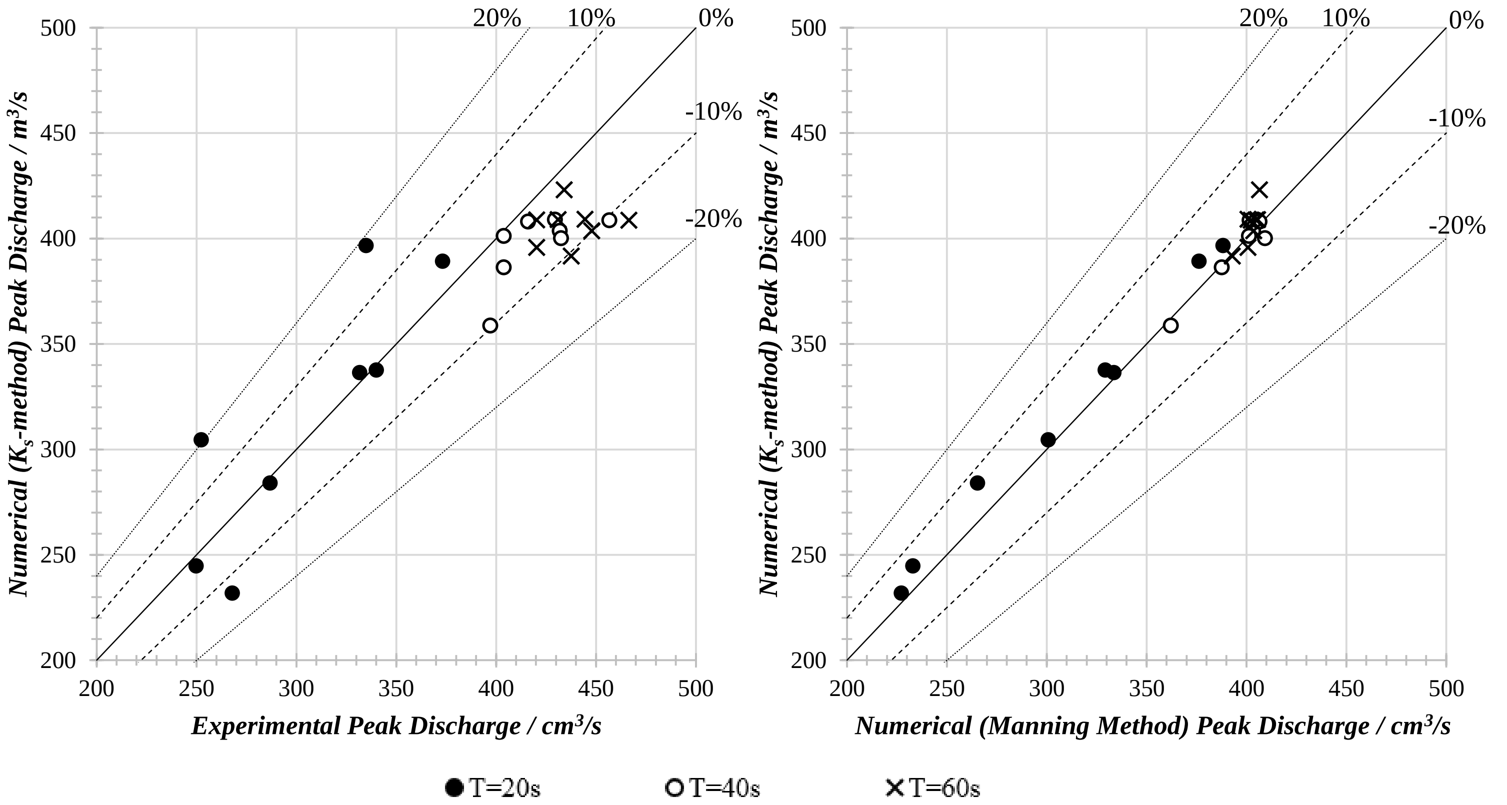

Figure 30: Experimental versus numerical peak discharges for all test cases. Line represents percentage deviation from perfect fit (solid line) (Left: peak discharge, Right: hydrograph width)

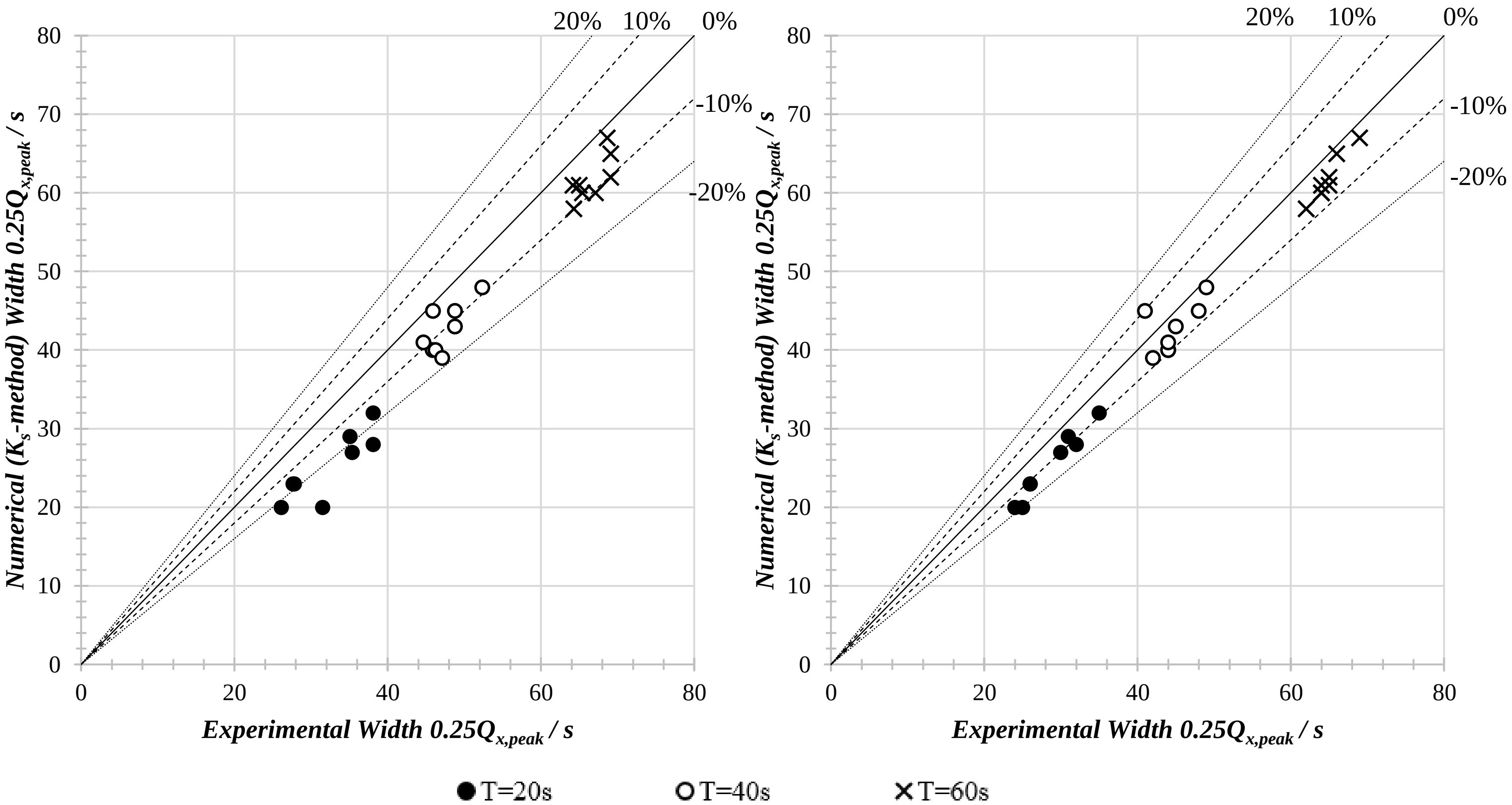

Figure 31: Experimental versus numerical hydrograph widths for all test cases. Line represents percentage deviation from perfect fit (solid line) (Left: peak discharge, Right: hydrograph width)

in time and space: the discharge value of 25 litres/minute was merely the estimated average value. Therefore, small fluctuations skewed experimental $Q_{x,peak}$ up.

Despite successfully predicting hydrograph widths of some cases accurately, the numerical k_s model underestimated the widths in other cases. Two plausible reasons were that surface tension delayed the onset of rising hydrographs in actual occasions and the leakage of nozzles after they were turned off prolonged the descending limbs.

Regarding computational efficiency and stability, the computation time taken by the numerical model using k_s-method was slightly higher as compared to using Manning method. Additional computational time was required to perform iterations in the Colebrook White type formula to obtain the Chezy coefficient U once the flow exceeded the Re threshold for laminar flow regime.

5. Parametric Study

The numerical model was applied to investigate the effects of building area ratio BA to the time of concentration T_c under a uniform rainfall lasted indefinitely (Chapter 1.4). Three typical building arrangement on a uniform slope was considered: regular, staggered and random.

5.1 Choice of resolution and catchment

Physically, as rainfall runoff gushes down the slope, some flows are obstructed by the presence of buildings; water accumulates and water depth increases in front of the building as kinetic energy is converted to potential energy. The obstructed stream gets diverted around the buildings; owing to the large momentum in the direction parallel to the upstream wall, a boundary is created at two sides of a building. Once the flow emerges from two sides, it merges into one stream again, but this process creates some reverse flow at the back of the building (Figure 32).

In the numerical model, all these features will need to be captured to more accurately predict the runoff discharge over time. This can be achieved by ensuring the side length of any building to be above 10 grid points (Lam, 2016). For a square catchment of 4.86 metres side length with 100 square buildings that occupy about 5% of total catchment area, the area of each building is about $0.012\ m^2$, which translates to the side length of each building of about 0.11 metres. Using a grid resolution $\Delta x = 0.01\ m$ would generate 11 grid points to represent the side length, which is sufficient. Hence, subsequent Δx is set to be $0.01\ m$.

Previous research also confirmed that choosing a small local area in numerical analysis would yield similar results to choosing larger area that consists of repeated tiles of the small areas (Lam, 2016). This can be used to increase computational efficiency in modelling large area with repeating building arrangement.

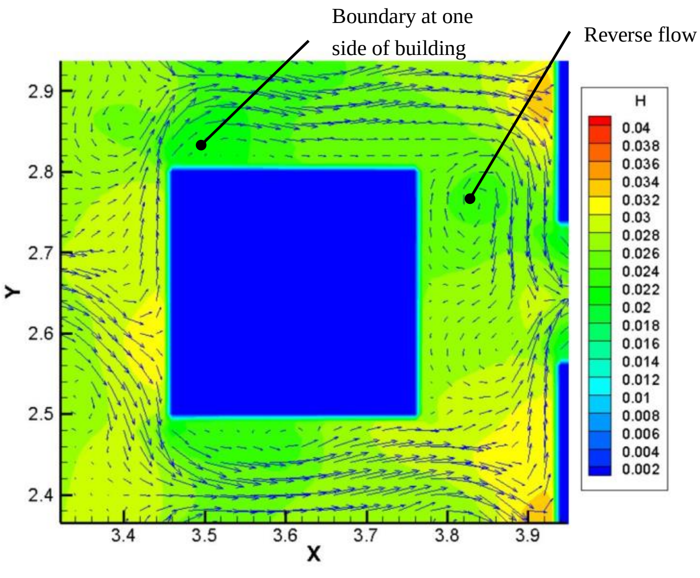

Figure 32: Flow around a square building (BA 40%, staggered)

5.2 Simulation parameters

In this project, square buildings were arranged in either regular, staggered or random layouts on a uniform slope s_b of 0.01. In particular, staggered matrices were designed to look identical when viewed from both x-axis and y-axis (Figure 33).

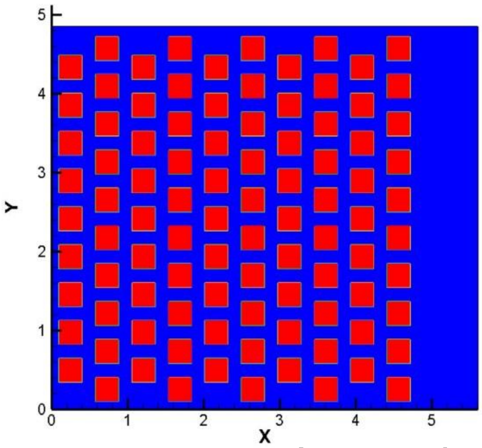

Figure 33: Staggered matrices with runoff leeway ($x > 4.86m$); buildings are shown in red

Size of the main domain was fixed to $4.86\ m \times 4.86\ m$. As the numerical nodes are finite, it was not possible in certain cases to place all buildings at where they are supposed to be in both regular and staggered matrices. Therefore, the buildings were placed at the closest square grids. An additional 60 metres of runoff leeway (equivalent to length of 60 grid points) of slope 0.02 was added at the downstream edge of the main domain.

To generate the topographic conditions for each numerical node, a Matlab script written by Lam (2016) was used; it allowed users to specify the building patterns and size of buildings. These were the only two independent variables in the subsequent sections.

Roughness of the terrain was modelled by directly setting the Chezy coefficient $U = 10^{30} m^{0.5}/s$. Rainfall intensity i is set to be $1 mm/s$ within the main domain excluding areas occupied by buildings as BH method was used.

5.3 Time of concentration T_C

While the concept of T_C is theoretically sound (Chapter 2.1), it is difficult to measure in a hydrograph produced using numerical method, as the latter often creates round-off errors and truncation errors; the numerical hydrographs will have some fluctuations, even after the actual T_C. While other researchers used the time to reach 25% or 50% of saturated flow to characterise T_C, Lam (2016) used the time reaching 70% of expected saturated flow T_{70} instead, noting the additional benefit of having bigger variation of T_{70} values for different scenarios (Figure 34). Therefore, T_{70} was adopted for subsequent simulations for the convenience of results comparison.

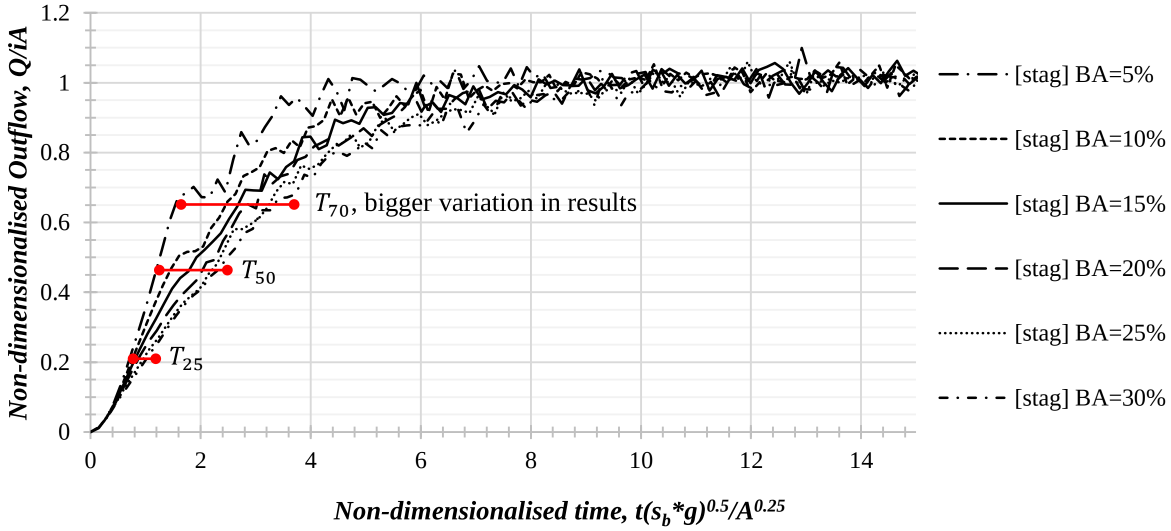

Figure 34: Non-dimensionalised hydrographs for terrain with 100 buildings arranged in staggered matrix (Area of catchment excluding BH is denoted as A, gravitational pull is denoted as g)

To obtain T_{70}, the instance when the hydrograph first registered outflow beyond 70% is recorded. The actual T_{70} is predicted using linear interpolation between this point and the previous data point. Inevitably, local fluctuations of hydrographs may affect the T_{70} values, which had to be considered in the analysis of the result.

5.4 Studied cases

To study the influence of building area ratio (BA) in detail, numerical simulations were performed on BA ≅ 5%, 10%, 20%, 30% and 40%. The actual BA was not whole number percentage as the size of the building had to be quantised to the nearest grid size Δx (i.e. 0.01 m). Given a BA value, there is only one possible regular and staggered building arrangement, but there are countless ways in which buildings can be arranged randomly. In order to gather sufficient samples to study the characteristics of T_{70}, 20 random building matrices were tested for each BA aforementioned. Further simulations on BA ≅ 15% and 20% were performed for staggered array to refine the results.

The study ceased beyond BA ≅ 40% as some randomly arranged buildings started forming clusters with tiny or no gap. Water may not reach the downstream as stream of runoff was blocked off by these dam-like buildings (Figure 35). Such dense build-up is unusual even in centre of a huge metropolitan, and hence was not studied subsequently.

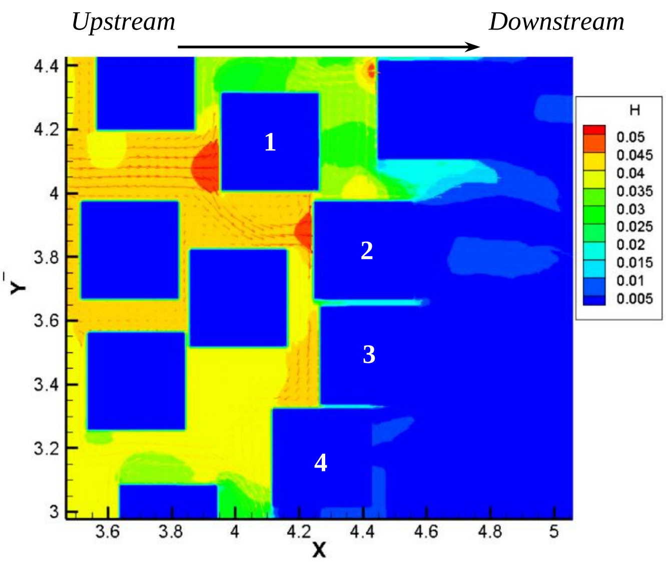

Figure 35: Buildings 1 to 4 blocked off rainwater discharge

5.5 Results

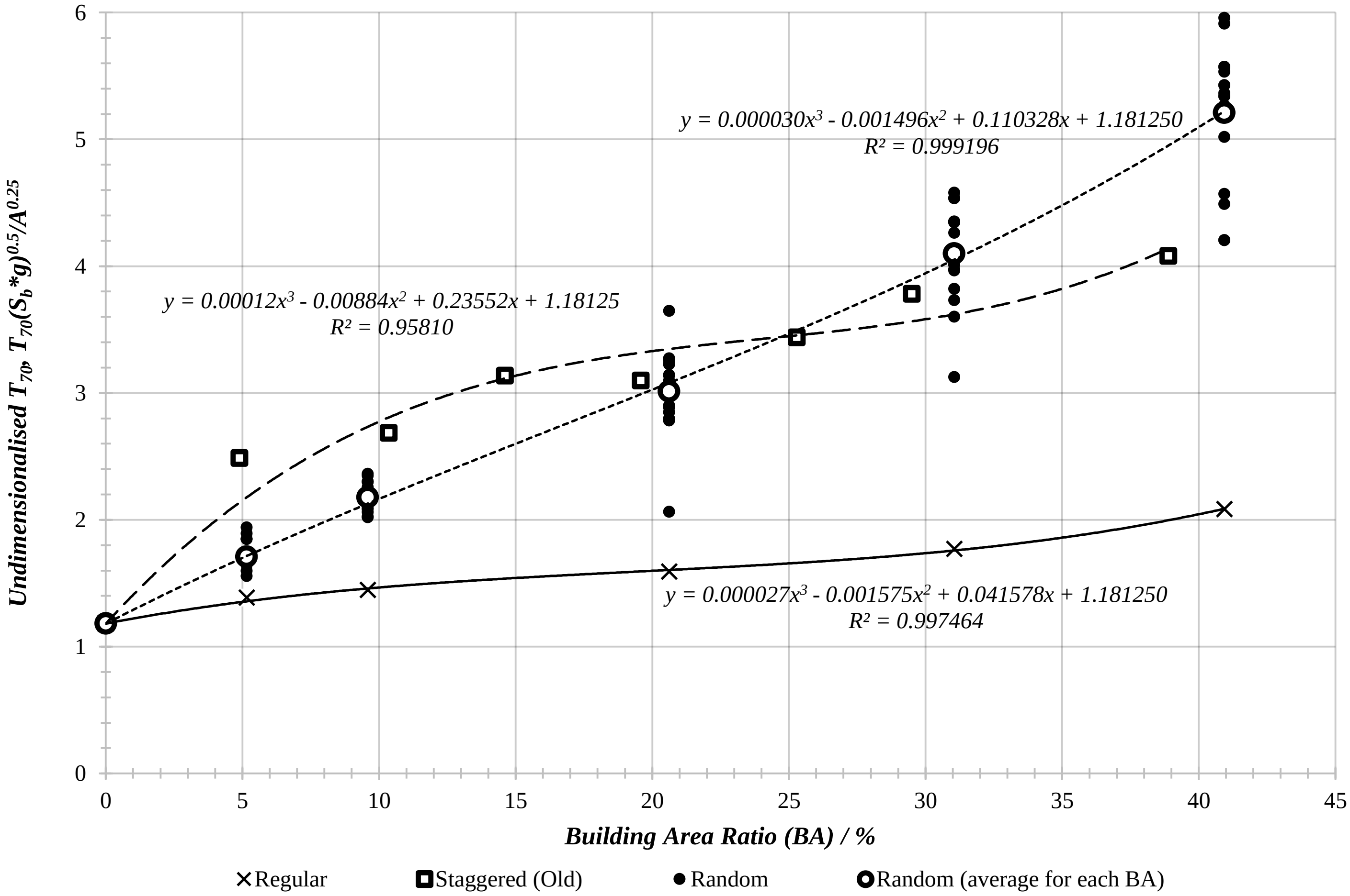

Figure 36: Effect of BA on the non-dimensionalised T_{70} for matrices for 100 buildings

Overall, the results conform to general expectations: given a fixed type of building arrangement, the larger the size of each building, the longer it takes for outflow rate to reach 70% of the volumetric rate of rainfall, inferring a higher the time of concentration T_C. The only anomaly to this trend happened when BA increased from 15% to 20% for staggered matrices (Figure 36); it was the result of local fluctuations near T_{70} of the two hydrographs (Figure 34).

Further comparison of T_{70} between different building matrices revealed interesting results. Once T_{70} diverged from 0% BA, it became clear that regular matrices consistently produced the lowest T_{70}. This was intuitive considering that building obstacles in staggered matrices were more spread out, hence blocking a larger area of runoff as compared to buildings in regular matrices; the latter was very effective in discharging runoff as buildings at downstream were placed right behind the buildings at upstream, hence minimising the number of times in which runoff streams ran into buildings (Figure 37). Therefore, less blockage increased the overall speed of runoff in downstream direction and reduced the length of flow paths.

While staggered matrices had longer T_C than most random matrices at low BA, its effectiveness in discharging rainfall improved as BA increases, up to the point where it achieved T_C before almost all random matrices at 40% BA. The observation at low BA conformed to the fact that there was plenty of space for a new small random building to develop in the terrain at small BA. Hence, it was likely that neighbouring buildings were far apart; sufficient gaps allowed runoff to pass. Even in areas where buildings were placed near each other randomly, the buildings were very small; large area of runoff streams remained unobstructed (Figure 38). Hence, T_C was relatively insensitive to gap sizes at small BA. On other hand, it was suspected that the blockage effect mentioned in the previous paragraph dominated T_C delay at low BA; staggered buildings were designed to spread intentionally, which had a higher probability to create more blockage than randomly placed buildings. Hence, T_C for staggered array was higher than that for random array at BA below 25%.

The observation beyond 25% BA was attributed to the increasing probability of random matrices forming building clusters in between buildings as BA increased (Figure 38). This severely affected the effectiveness of discharging runoff as the runoff was trapped within this clusters when the available discharge gaps were small (Figure 35). Therefore, gap size was a prominent factor at high BA.

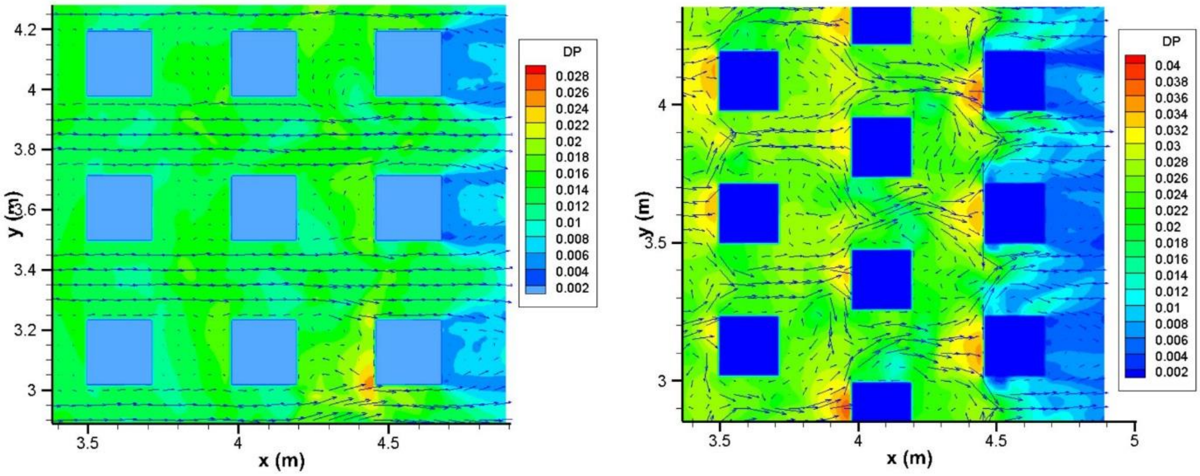

Figure 37: More severe blockage effect in staggered array (right) as compared to regular array (left)

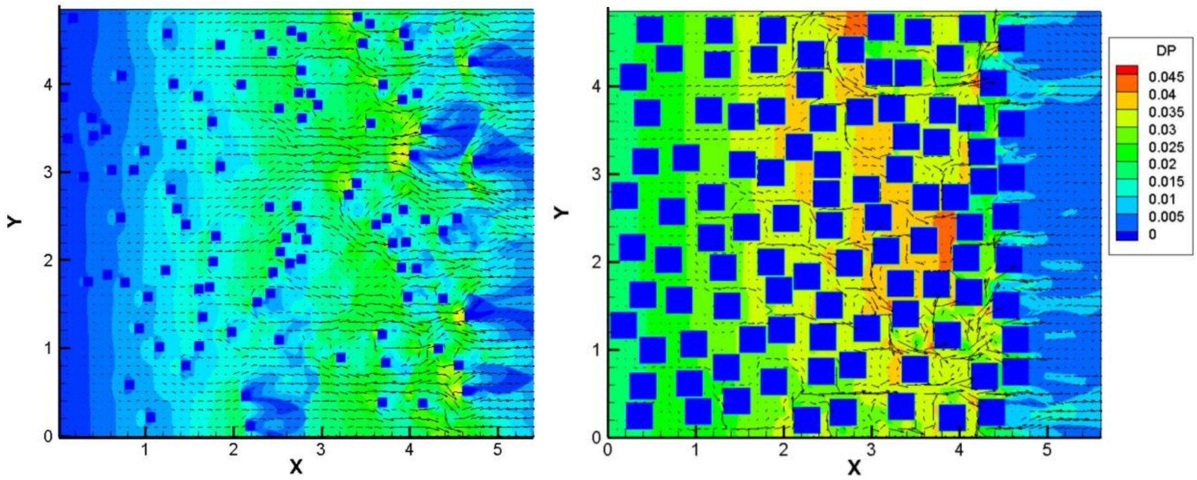

Figure 38: Unobstructed flow in small BA (left) versus congested flow in large BA (right) for random array

Another interesting point was the shape of the best-fit curves. Lam (2016) conducted simulations up to 30% BA and suggested quadratic fit to staggered array and linear fit to regular and random array (Chapter 1, Figure 3). However, those curves consistently underestimated T_{70} at 40% BA.

Close examination of results suggested that all best-fit curves were divided into two segments: at low BA, the curves should concave downward $\left(\frac{d^2y}{dx^2} < 0\right)$; at high BA, it should concave upward $\left(\frac{d^2y}{dx^2} > 0\right)$. Therefore, cubic functions were selected for best fits, with the following inflection points $\left(\frac{d^2y}{dx^2} = 0\right)$ (Table 7).

Building Array	**BA / %**
Regular	19.4
Staggered	24.6
Random	16.6

Table 7: Inflection points for best-fit curves of each building array shown in Figure 36

The presence of inflection points possibly suggested two governing factors acting at different range of BA. In an attempt to justify the shape of these best-fit functions, the following section focused on the effect of blockage and overall gap size on T_{70}.

5.6 Effect of blockage on T_C

For staggered and regular matrices, the position of the buildings was fixed; increasing BA would increase the size of building. Therefore, larger portion of runoff was blocked off by buildings. This phenomena was suspected to dominate the variation in T_C for low BA in the previous section.

Mathematically, for a square terrain of total plan area A_T with N square buildings, its side length side L can be expressed as

$$L = \sqrt{\frac{A_T \times BA}{N}}$$

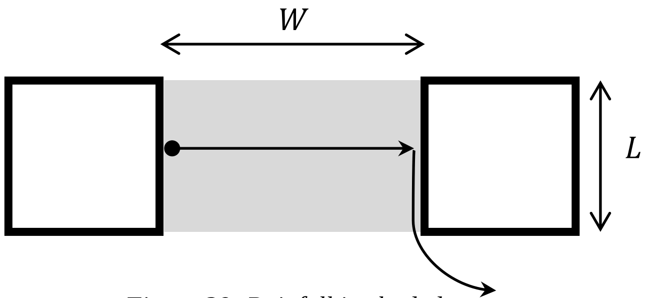

Figure 39: Rainfall in shaded area was affected by building

In a regular array, assuming a correlation between the delay of time of concentration ΔT_C and the total area of rainfall in the domain being affected by the buildings A_R (one such area was shaded in grey in Figure 39), then for all buildings,

$$\Delta T_C \sim A_R \quad A_R = NLW = W\sqrt{A_T \times BA \times N}$$

where W denoted how far downstream the adjacent building was. However, W was dependent on BA. Since the size of whole domain was $\sqrt{A_T}$, it could then be inferred that

$$W \approx \frac{\sqrt{A_T} - \sqrt{A_T \times BA}}{\sqrt{N}} \qquad \textit{Equation (5)}$$

$$\Delta T_C \sim A_T\sqrt{BA}(1 - \sqrt{BA})$$

For staggered arrays, there were twice as many rows of buildings. Therefore, $A_S = 2A_R$. By plotting A_S and A_R versus BA (Figure 40), one could identify two features that were similar to those cubic functions (Figure 36): the curves that concaved downward and the position of turning point at 25% BA, which was not far from those BA of inflection points (Table 7).

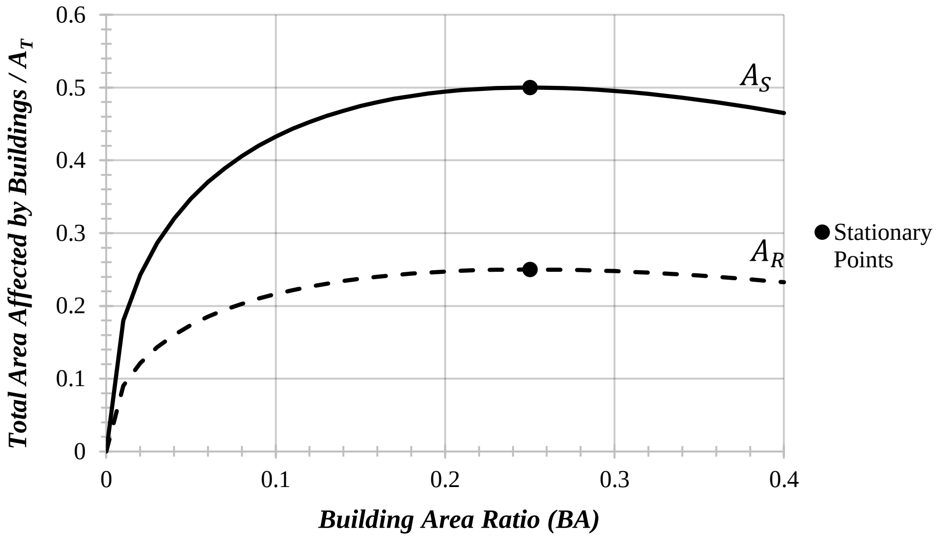

Figure 40: A_S and A_R versus BA

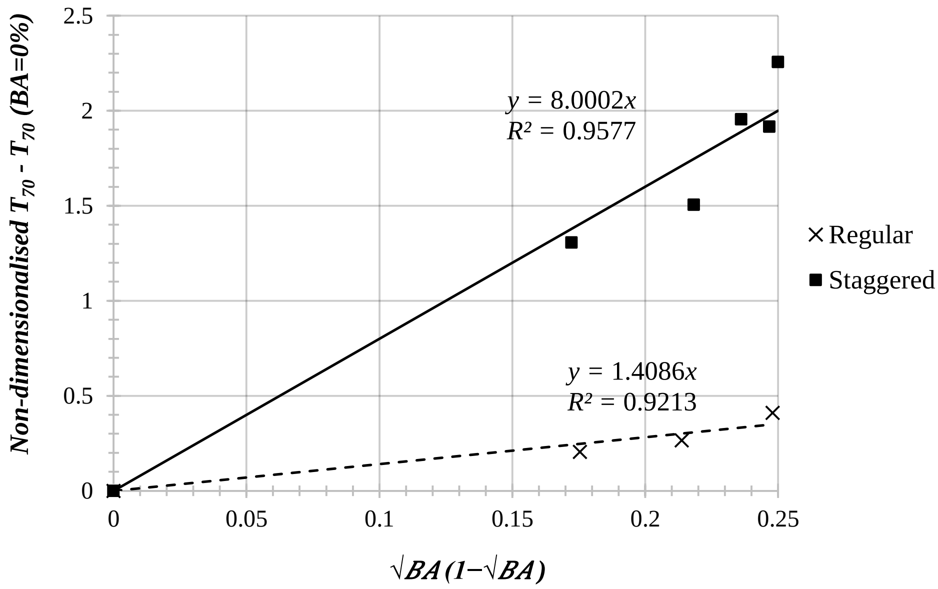

Figure 41:Fitting non-dimensionalised ΔT_{70} to $\sqrt{BA}(1-\sqrt{BA})$ for regular and staggered arrays for BA < 25%

If the results of regular and staggered arrays for BA < 25% were then used to be plotted against $\sqrt{BA}(1-\sqrt{BA})$, a common factor for both A_R and A_s (Figure 41), there were good linear correlation with strong R^2 values for both types of arrays. Although $A_S = 2A_R$, the gradient of staggered fit was 5.7 times higher than that of regular. This seemed to suggest that, for low BA, the effect of blockage quantified above was suitable to explain the variation in T_C within the same type of array. Nonetheless, the relationship above could not be generalised to other types of arrays.

5.7 Effect of gap sizes on T_C

For regular array, the gap between two buildings, W was previously found in Equation 5. Although staggered matrices had twice as many rows, the columns alternated, and hence the gap between two adjacent buildings was essentially the same. Since both arrays had $\sqrt{N}$ gaps, the combined width of the gap W_T were

$$W_{T,Regular} \approx W_{T,Staggered} \approx \sqrt{A_T}\left(1 - \sqrt{BA}\right)$$

for any cross sectional cut along plane perpendicular to the direction from upstream to downstream (x-plane). In addition, boundary flow observed in Chapter 5.1 suggested that the effective width of the flow was smaller than the actual width: an additional factor z with value larger than 1 could be multiplied to the actual size of the building $\sqrt{BA}$ to further narrow the gap.

It was known that the volumetric discharge rate Q_x of any given rectangular channel could be obtained by using formula

$$Q_x = W_T H U_x$$

where H is the water depth and U_x is the velocity of flow in the downstream (x-)direction. For a fixed total volume of rainfall V onto a domain, the time T required to completely discharge all rainfall can be loosely approximated using

$$T \sim \frac{V}{Q_x} = \frac{V}{HU_x} \times \frac{1}{\sqrt{A_T}\left(1 - z\sqrt{BA}\right)}$$

Therefore, it was assumed that a correlation between T_C and $\left(1 - z\sqrt{BA}\right)^{-1}$ existed. By plotting $\left(1 - z\sqrt{BA}\right)^{-1}$ versus BA, it was clear that all the curves were upward concave (Figure 42); as the effective width became narrower, its effect on T_C could become stronger. This could explain the variation in non-dimensionalised T_{70} at higher BA values, particularly the best-fit of staggered array.

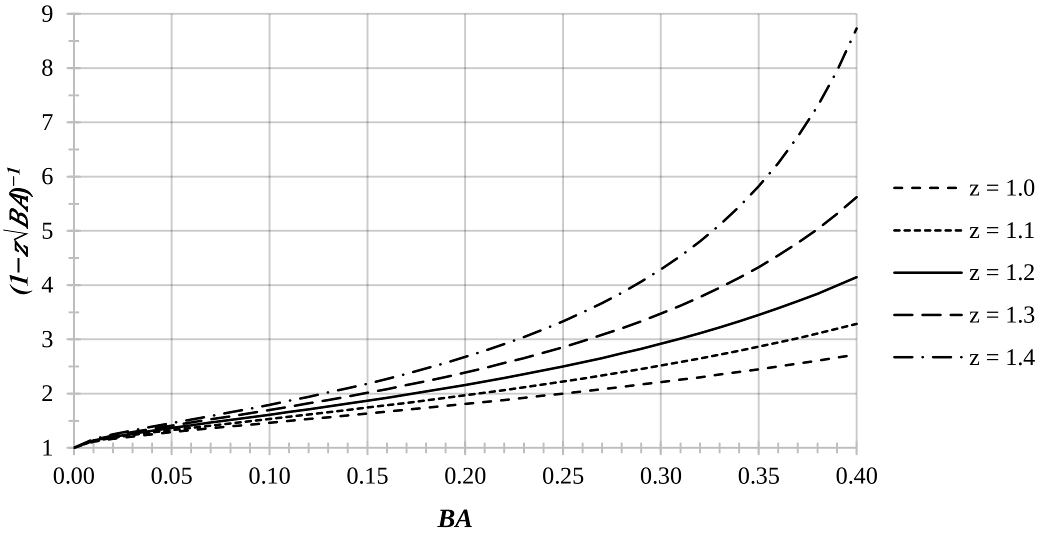

Figure 42: Increasing effect of gap sizes at higher BA

5.8 T_C in random array

While the blockage and narrow gap effects aforementioned were still relevant, there are more factors that affect T_C of random array. Given a fixed BA, T_C could vary considerable depending on how buildings were distributed spatially; if larger number of the 100 buildings were placed closer to the top of the slope (i.e. upstream), T_C would likely be lower as there was less obstruction at downstream, where almost all runoff discharge would have to pass through. Furthermore, BH method also implied that the 'centroid' of rainfall would be shifted closer to downstream when more buildings were at upstream; this effectively reduce the average distance rain droplets would need to travel to reach the outlet, further reducing T_C. Take, for instance, the comparison of layout between random arrays that yield maximum and minimum T_{70} (Figure 43 and Table 8).

The standard deviation of T_C was observed to be directly proportional to BA (Figure 43). One possible explanation attributed this spread to the increasing sensitivity of T_C towards how buildings were arranged at higher BA, which can be partially due to the increasing effect of gap sizes. Increasing the value of z slightly (Figure 42) produced a growing difference in $\left(1 - z\sqrt{BA}\right)^{-1}$ at higher BA. Therefore, at high BA, if buildings were arranged as far apart as possible such as those in regular and staggered arrays, the effective gaps was large, hence z could be thought to have a small value close to 1. On the contrary, if most buildings were congested in an area, effective gaps would be small.

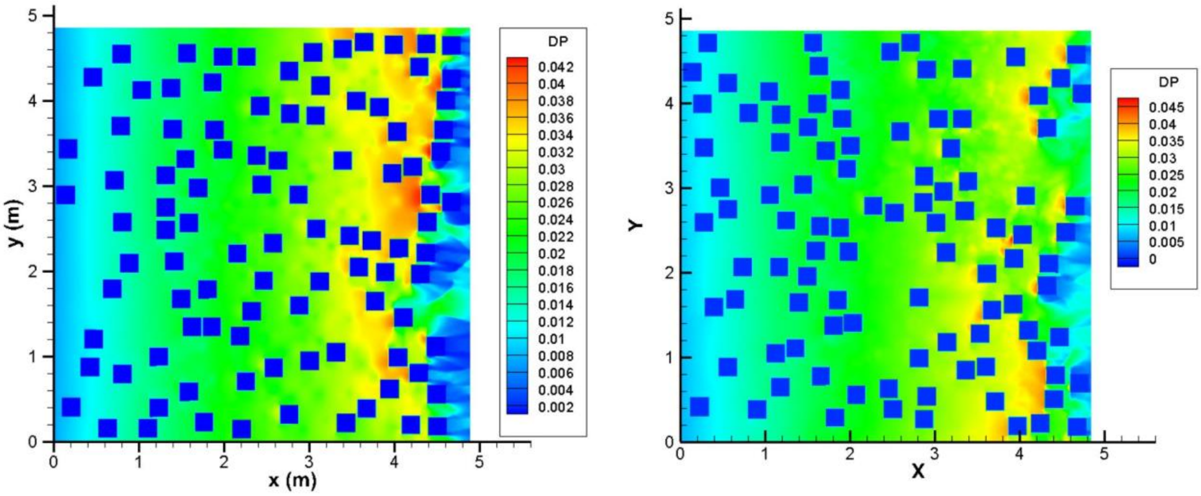

Figure 43: 100-building random layouts of 20% BA that yielded maximum T_C (left) and minimum T_C (right)

Random Layout (Figure 43)	**Left**	**Right**
T_{70}/s	24.2	13.7
Number of whole buildings at $x < 1m$	14	15
Number of whole buildings at $x < 2m$	36	41
Number of whole buildings at $x < 3m$	56	60
Number of whole buildings at $x < 4m$	76	77

Table 8: Distribution of buildings between the top and the bottom of the slope

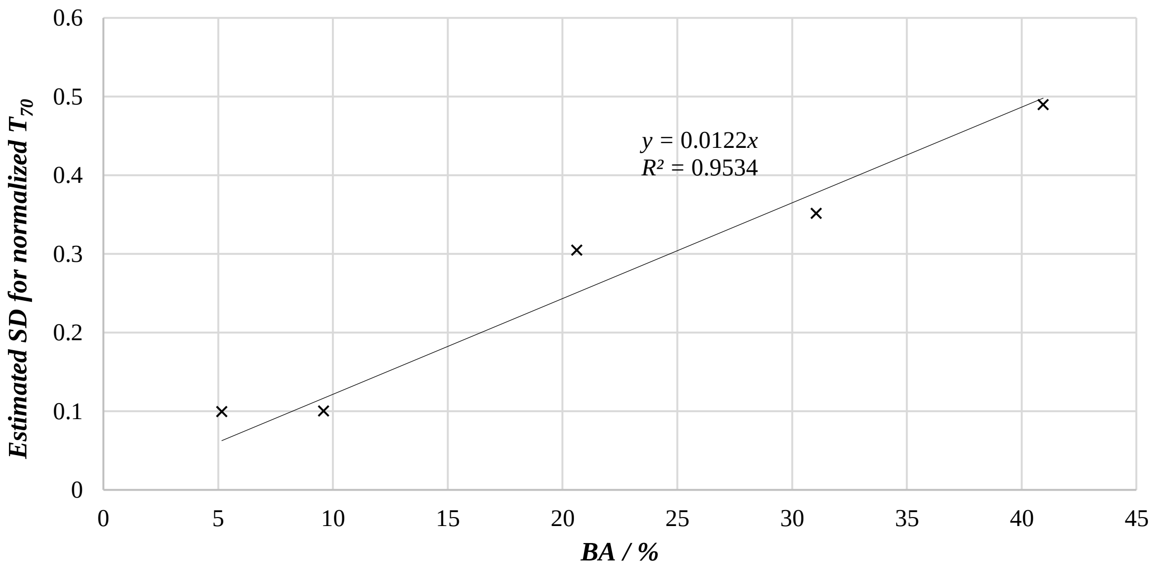

Figure 44: Increasing spread of T_{70} at higher BA

7. Conclusion

8. Future Work

8. References

Intro

https://www.eea.europa.eu/data-and-maps/figures/urban-flooding-2014-impervious-surfaces
http://ponce.sdsu.edu/the_kinematic_wave_controversy.html

Background

http://www.raingain.eu/sites/default/files/wp3_review_document.pdf

Model Improvement

http://www.vectortechengineering.co.uk/latest-news/how-to-use-a-moody-chart/

9. Appendixes

9.1 Derivation of relationship between resistance coefficient f and Reynolds number Re in laminar flow regime

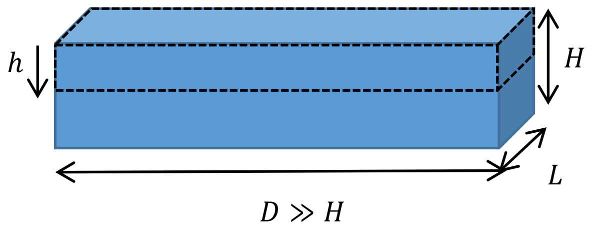

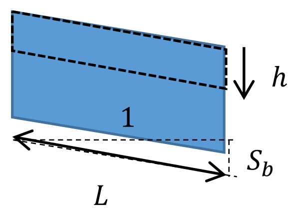

Assuming water is flowing along the direction parallel to L. The floodplain bed has a slope of 1: S_b and is very wide as compared to the flood depth. By balancing forces acting on the free body (dotted trapezoid), one can find that

$$\tau = \rho g R_h S_b \approx \rho g h S_b \qquad (1)$$

For Newtonian Fluid, $\tau = -\mu \frac{du}{dh}$ (negative sign because velocity decreases from the surface to the floodplain bed), hence

$$\frac{du}{dh} = -\frac{\rho g h S_b}{\mu} \qquad (2)$$

which can be integrated to give the velocity profile

$$u(h) = -\frac{\rho g S_b}{2\mu} h^2 + C_1 \qquad (3)$$

where C_1 is a constant. Because the fluid is viscous it sticks to the pipe wall so that $u(H) = 0$, hence

$$u(h) = \frac{\rho g S_b H^2}{2\mu}\left(1 - \frac{h^2}{H^2}\right) \qquad (4)$$

The volumetric flowrate q_v through the section can be obtained by integrating the velocity profile. Since the flow is uniform across D

$$q_v = D\int_0^H u(h)\, dh = \frac{\rho g S_b H^2 D}{2\mu}\left(H - \frac{H}{3}\right)$$
$$= \frac{\rho g S_b H^3 D}{3\mu} \qquad (5)$$

Average velocity is then

$$U = \frac{q_v}{DH} = \frac{\rho g S_b H^2}{3\mu} \qquad (6)$$

From Chézy formula,

$$\mu = C\sqrt{R_h S_b} = \sqrt{\frac{8g}{f}} \times \sqrt{R_h S_b}$$
$$\approx \sqrt{\frac{8HgS_b}{f}} \qquad (7)$$

HgS_b in Equation (7) can be expressed in variables ρ, μ, U and H by rearranging Equation (6). Substitute this form back into Equation (7) and rearrange gives

$$f = \frac{24}{\frac{\rho U H}{\mu}} = \frac{24}{Re_{depth}} = \frac{96}{Re_{diameter}} \qquad (9)$$

This relationship forms the basis for predicting Chézy coefficient in low Reynolds region, including those obtained from experiments.

9.2 Fortran code to set Chezy coefficient *U*

```
!       CALCULATE THE CHEZY VALUE
!       INPUT: IMAX,JMAX,ACT,DP,UM,VM,VARCHZ
!       METHOD: NFLCHZ (1-CONSTANT CHEZY, 2-MANNING METHOD, 3-Ks-METHOD)
!       OUTPUT:CHZ
! -----------------------------------------------------------------------
        SUBROUTINE CHEZY (IMAX, JMAX, ACT, DP, QX, QY, VARCHZ, NFLCHZ, CHZ)
        IMPLICIT NONE
        INTEGER,INTENT(IN) :: IMAX, JMAX, NFLCHZ
        LOGICAL,INTENT(IN) :: ACT(IMAX,JMAX)
        REAL(4),INTENT(IN) :: DP(IMAX,JMAX),QX(IMAX,JMAX),QY(IMAX,JMAX),VARCHZ(IMAX,JMAX)
        REAL(4),INTENT(OUT):: CHZ(IMAX,JMAX)

        INTEGER I, J
        REAL(4) RE, TTMP, CHZOLD, VISLAM0, TURBULENTB, LAMINARB, CHZUPPER, CHZLOWER
        VISLAM0 = 1.30E-6

        IF(NFLCHZ .EQ. 1) THEN
!           SETTING A CONSTANT CHEZY COEFFICIENT
            DO 100 I = 2, IMAX - 1
            DO 100 J = 2, JMAX - 1
                IF( ACT(I,J) )  CHZ(I, J) = VARCHZ(I,J)
100         CONTINUE

        ELSE IF(NFLCHZ .EQ. 2) THEN
!           MANNING METHOD
            DO 200 I = 2, IMAX - 1
            DO 200 J = 2, JMAX - 1
                IF( ACT(I,J) )  CHZ(I, J) = DP(I,J)**0.166667 / VARCHZ(I,J)
200         CONTINUE

        ELSE IF(NFLCHZ .EQ. 3) THEN
!           Ks-METHOD
!           SETTING UPPER LAMINAR REYNOLDS VALUE AND LOWER TURBULENT REYNOLDS VALUE
            TURBULENTB = 4000.0
            LAMINARB = 2000.0
            DO 300 I = 2, IMAX - 1
            DO 300 J = 2, JMAX - 1
                IF( ACT(I,J) ) THEN
                    RE = 4.0 * SQRT(QX(I,J)*QX(I,J)+QY(I,J)*QY(I,J)) / VISLAM0

!               TURBULENT REGION (COLEBROOK-WHITE FORMULA)
                    IF(RE .GT. TURBULENTB) THEN
                        TTMP = VARCHZ(I,J) / (DP(I,J)*12.0)
                        CHZ(I,J) = -18.0 * LOG10(TTMP)
350                     CHZOLD = CHZ(I,J)
                        CHZ(I,J) = -18.0 * LOG10(TTMP + 5.0/(RE*18.0)*CHZOLD)
                        IF( ABS(CHZ(I,J)-CHZOLD) .GT. 0.5 )   GOTO 350

!               LAMINAR REGION
                    ELSEIF(RE .LT. LAMINARB) THEN
                        IF( RE .LT. 0.1) RE = 0.1
                        CHZ(I, J) = SQRT(RE*5/6)

!               TRANSITION REGION, USING LINEAR INTEPOLATION BETWEEN LAMINAR AND TURBULENT
                    ELSE
                        TTMP = VARCHZ(I,J) / (DP(I,J)*12.0)
                        CHZUPPER = -18.0 * LOG10(TTMP)
360                     CHZOLD = CHZUPPER
                        CHZUPPER = -18.0 * LOG10(TTMP + 5.0/(TURBULENTB*18.0)*CHZOLD)
                        IF( ABS(CHZUPPER-CHZOLD) .GT. 0.5 )   GOTO 360
                        CHZLOWER = SQRT(LAMINARB*5/6)
                        CHZ(I,J) = ((RE-LAMINARB)*CHZUPPER + (TURBULENTB-RE)*CHZLOWER) / (TURBULENTB - LAMINARB)
                    END IF
                END IF
300         CONTINUE
        END IF

        RETURN
        END
```

9.3 Risk Assessment Retrospect

As identified in the initial risk assessment, the major risk associated to myself was the health risk caused by prolonged use of computers. This included bad posture when sitting and typing, soreness of eyes under extended duration of exposure to digital screens and lack of physical movement when working over hours. Such risks would be more compounded when deadlines were approaching and the person was psychologically pressured. The risks easily be overlooked in retrospect.

Mitigations had been made throughout the project by phasing out work, during the year and during the day. Outside necessary time of data processing and documentation, time of exposure to computers or sitting was reduced. Regular exercises also allowed muscles to stretch and pressure to relieve. Improvements would enable better care when completing similar projects in the future.